COMPUTER ASSISTED DETECTION OF POLYCYSTIC OVARY MORPHOLOGY IN ULTRASOUND IMAGES

A Thesis Submitted to the
College of Graduate Studies and Research
in Partial Fulfillment of the Requirements
for the degree of Master of Science
in the Division of Biomedical Engineering
University of Saskatchewan
Saskatoon

By
Maryruth Pradeepa Raghavan

PERMISSION TO USE

In presenting this thesis in partial fulfilment of the requirements for a Postgraduate degree from the University of Saskatchewan, I agree that the Libraries of this University may make it freely available for inspection. I further agree that permission for copying of this thesis in any manner, in whole or in part, for scholarly purposes may be granted by the professor or professors who supervised my thesis work or, in their absence, by the Head of the Department or the Dean of the College in which my thesis work was done. It is understood that any copying or publication or use of this thesis or parts thereof for financial gain shall not be allowed without my written permission. It is also understood that due recognition shall be given to me and to the University of Saskatchewan in any scholarly use which may be made of any material in my thesis.

Requests for permission to copy or to make other use of material in this thesis in whole or part should be addressed to:

Head of the Division of Biomedical Engineering
Room 2A20 Engineering Building
57 Campus Drive
University of Saskatchewan
Saskatoon, Saskatchewan
Canada
S7N 5A9

ABSTRACT

Polycystic ovary syndrome (PCOS) is an endocrine abnormality with multiple diagnostic criteria due to its heterogenic manifestations. One of the diagnostic criterion includes analysis of ultrasound images of ovaries for the detection of number, size, and distribution of follicles within the ovary. This involves manual tracing of follicles on the ultrasound images to determine the presence of a polycystic ovary (PCO). A novel method that automates PCO morphology detection is described. Our algorithm involves automatic segmentation of follicles from ultrasound images, quantifying the attributes of the segmented follicles using stereology, storing follicle attributes as feature vectors, and finally classification of the feature vector into two categories. The classification categories are PCO morphology present and PCO morphology absent. An automatic PCO diagnostic tool would save considerable time spent on manual tracing of follicles and measuring the length and width of every follicle. Our procedure was able to achieve classification accuracy of 92.86% using a linear discriminant classifier. Our classifier will improve the rapidity and accuracy of PCOS diagnosis, and reduce the chance of the severe health implications that can arise from delayed diagnosis.

ACKNOWLEDGEMENTS

I would like to sincerely thank my supervisors Dr. Roger Pierson, Dr. Mark Eramian, and Dr. Eric Neufeld for their financial help, unwavering guidance, support, and encouragement throughout my graduate studies. I would also like to thank my committee members for their suggestions and support. My special thanks to the Department of Computer Science for providing a friendly and pleasant environment to do my research. I take this opportunity to thank my friends for their encouragement throughout my studies. Finally, I am very grateful to my family for their love, encouragement and support throughout this work.

CONTENTS

LIST OF TABLES

LIST OF FIGURES

LIST OF ABBREVIATIONS

SVM	Support Vector Machines
KNN	K-Nearest Neighbor
PCOS	Polycystic Ovary Syndrome
PCO	PolyCystic Ovary
FSH	Follicle Stimulating Hormone
LDC	Linear Discriminant Classifier
VD	Volume density
SD	Surface density
HDist	Hausdorff distance
MDist	Mean distance
RR	Recognition rate
MR	Misidentification rate

CHAPTER 1

INTRODUCTION

1.1 Motivation

1.1.1 Overview of PCOS

Polycystic Ovary Syndrome (PCOS) is an endocrine and metabolic abnormality that affects 5-10% women of reproductive age [13]. It is a condition that is comprised of heterogenous symptoms making it difficult to establish consistent diagnostic criteria based on a single biochemical/clinical assessment. Some of the symptoms exhibited by women with this condition are menstrual irregularity, anovulation or oligoovulation, obesity, infertility, and hyperandrogenism that presents as acne, male pattern baldness, and male pattern hair growth. The diagnostic criteria for PCOS were originally established by two different bodies; the ESHRE (European Society of Human Reproduction and Embryology), and the ASRM (American Society of Reproductive Medicine). The ESHRE criteria required the presence of polycystic ovaries on an ultrasonographic examination in addition to symptoms of hyperandrogenism and anovulation/oligoovulation. It also required the absence of any pituitary or adrenal disease [14]. The ASRM criteria required clinical signs of hyperandrogenism and ovulatory abnormality in the absence of adrenal hyperplasia (impairment of a key enzyme in the production of cortisol and aldosterone by the adrenal gland). It did not require ultrasonographic examination of the ovaries. This disparity has now been resolved and the diagnostic criteria of PCOS have been jointly redefined by ASRM and ESHRE in an international consensus meeting as the presence of at least two of the following three criteria: 1) Oligo or anovulation; 2) biochemical and/or clinical signs of hyperandrogenism; and, 3) the presence of at least one polycystic ovary on an ul-

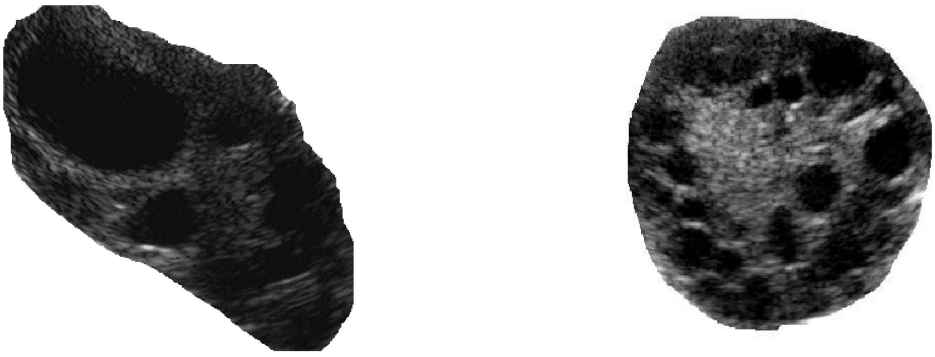

Normal ovary Polycystic ovary

Figure 1.1: Example of normal and polycystic ovaries

trasonographic examination. A polycystic ovary (PCO) is one that is characterized by the presence of 12 or more follicles measuring around 2-9 mm in diameter and/or measured ovarian volume of $> 10\ cm^3$ [1].

Analysis of ultrasonographic images for detecting follicle morphology is an important diagnostic marker in the refined definition of PCOS as per the international consensus criteria. Hence, ultrasonographic imaging of the ovaries is included in routine checkups for menstrual abnormalities, infertility treatments, and/or hyperandrogenic symptoms. Figure 1.1 shows ultrasonographic images of a normal ovary and a polycystic ovary. In a normal ovary the follicle count is lesser than in a polycystic ovary, and the follicles exhibit a random distribution within the ovary. Alternatively, polycystic ovaries exhibit more smaller, possibly irregularly shaped follicles, and, in most of the cases, a peripheral distribution of follicles.

A decision as to whether a patient has PCO or not is made by counting the number of follicles, determining the size (diameter) of each follicle and/or calculating the ovarian volume. This is a subjective process, and is highly dependent on the experience and proficiency of the ultrasonographer. Even though expert decisions are reliable, an automation of the process would minimize the subjectivity of the analysis, the interobserver variability that may arise, the need to convert between national/international standardizations, and

the fatigue that could happen when reading numerous images every day. It would also increase the number of images that can be analyzed per day thereby increasing the number of patients that can be handled on a day to day basis as well as improving the accuracy with which the images can be interpreted. It could provide the patient with a quick response time allowing them to seek medical advice/treatments quickly that may abate or obviate the severe consequences of the disease. The healthcare system could also benefit by this quick response time. This not only off-loads the strenuous work from the imaging specialist, but could also prove to be economically beneficial to the Heath Care systems of federal and provincial Governments.

1.2 Goals and Challenges

Our objective was to test the hypothesis that PCO morphology can be detected effectively ($> 90\%$) in ultrasonographic images using an automated image analysis technique. Our work aims to automate the analysis of pelvic ultrasonographic images for detecting PCO morphology by examining the number, size, and distribution of follicles within the ovary. Automation of the analysis of pelvic ultrasonographic images was achieved using a three step process that involved: 1) Segmentation of follicles from the ultrasonographic images using image processing methods; 2) application of a mathematical methodology called stereology to quantify the attributes of the segmented follicles and store them as feature vectors; and, 3) classifying the feature vector obtained from the previous step into one of the two categories: PCO morphology present or normal. These are the three key steps that form the basis of the automatic PCO morphology detection system. We faced some challenges to accomplish this automatic detection as ultrasonographic images are noisier than images obtained from other modalities due to the physics of acoustic imaging. Also, in ultrasonographic images the borders of follicle regions may not be well defined due to artifacts such as reverberation and acoustic shadowing/enhancement, which makes it difficult for a follicle segmentation algorithm to interpret the exact border. For this reason, the regular thresholding techniques or the edge detection methods that perform segmentation do not give acceptable results.

1.3 System Architecture

This software system is divided into three modules: 1) Fully automated follicle segmentation; 2) quantification of follicle morphology; and, 3) classification of follicle morphology. The novelty of our method lies in the amalgamation of the follicle segmentation technique with the stereological methodology from which a feature vector quantifying the ovarian morphology can be derived. The first module segments the follicle based on Potočnik and Zazula's [2] fully automated follicle segmentation algorithm, the second module quantifies the segmented follicles using stereology to derive the feature vectors, and the final module classifies the feature vectors using a linear discriminant classifier, support vector machine (SVM) classifier, and k nearest neighbor classifier (KNN).

1.4 Thesis Organisation

Chapter 2 of the thesis gives a general background of reproductive biology to present the reader with a clear understanding of ovarian and follicle morphology. Brief introductions to the physics of ultrasonography and principles of stereology are also presented.

Chapter 3 discusses previous work in the analysis of ovarian ultrasonographic images. Algorithms for analyzing follicle/ovarian morphologies, and techniques for analyzing tissue characterization of ovarian abnormalities are discussed. It also briefly discusses the different classifiers used for the classification of feature vectors.

Chapter 4 gives a detailed description of the methodology adopted to achieve automatic analysis of PCO morphology and includes description of the automated follicle segmentation, stereology, and classification including cross validation techniques. The problem of detecting the overall spatial distribution of follicles in the ovary is also discussed. Two types of distributions are possible: Peripheral distribution and random distribution. In peripheral distribution, follicles are distributed along the periphery of the ovary. In a random distribution, follicles are distributed in a random fashion within the ovary. Normal ovaries usually present a random distribution and may exhibit one or two "dominant" follicles which, by definition, are at least 2-3mm larger than the rest. Polycystic ovaries typically

exhibit a more peripheral distribution pattern, although there are notable exceptions.

Results of our experiments with details on the performance analysis are presented in Chapter 5. Conclusion and future work are discussed in Chapter 6.

CHAPTER 2

BACKGROUND

2.1 Human Ovarian Physiology

The main organs of the female reproductive system are the uterus, ovaries, and the fallopian tubes. Figure 2.1 shows the organs of the female reproductive system. The uterus is a hollow muscular organ which houses the fertilized egg and is the site of gestational development until birth. Ovaries are roughly ellipsoidal strucutures housed on either side of the uterus and are the master organs of the female reproductive system. They are responsible for the secretion of the reproductive hormones estrogen and progesterone, and for the production, storing, and release of the ovum or the mature egg. Each ovary measures approximately 3 cm x 1.5 cm x 1.5 cm in an adult woman. The fallopian tubes, through which the mature egg or the ovum travels to reach the uterus extend from the ovary to the upper part of the uterus [5].

The ovum develops inside a follicle in an ovary. An ovary contains a few hundred thousand primordial (microscopic) follicles at birth; only around 400 follicles develop into a preovulatory follicle (mature/dominant follicle) in an adult woman's lifetime [15]. At given times, a cohort of follicles are chosen for maturation. The chosen follicles grow from the initial stage in which they are called primordial follicles into the final stage in which they are called preovulatory follicles reaching up to a size of 20 mm to 25 mm. Hence, the ovary at anytime has follicles in several different stages of development [16]. The chosen cohort of follicles compete with one another for FSH (Follicle Stimulating Hormone) for physiologic dominance. One follicle can become dominant and ovulate. The growth of the other competing follicles is inhibited and they die. This type of programmed follicle death is called atresia. Once the ovum is released from the mature follicle, remnants

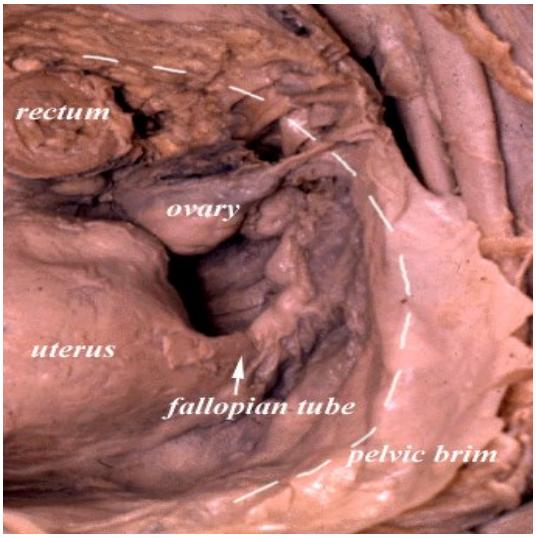

Figure 2.1: Main organs of female reproductive system showing ovary, uterus, and fallopian Tube [5]

of the ruptured follicle becomes a corpus luteum. The stages of a follicle life cycle or folliculogenesis is shown in Figure 2.2. If this cycle is disrupted, ovulation would be affected which might lead to infertility and/or other forms of ovarian abberation [17].

Polycystic Ovary Syndrome (PCOS) is an abberation in the ovarian function that results in irregularities where no follicle from the cohort of chosen follicles can develop into a mature follicle capable of ovulation. Since there is no dominant follicle, atresia or follicle death of the competing follicles does not occur. This syndrome gets its name polycystic from the "cystic" appearance of the multiple follicles that were unable to develop into a dominant follicle. Figure 2.4 shows polycystic ovaries and ultrasonographic images of polycystic ovaries.

2.2 Polycystic Ovary Syndrome

2.2.1 PCOS causes: Hypotheses

Polycystic ovary syndrome affects 5 to 10 % of women of reproductive age [13]. Some of the theories that have been proposed as the underlying cause of PCOS are aberrations

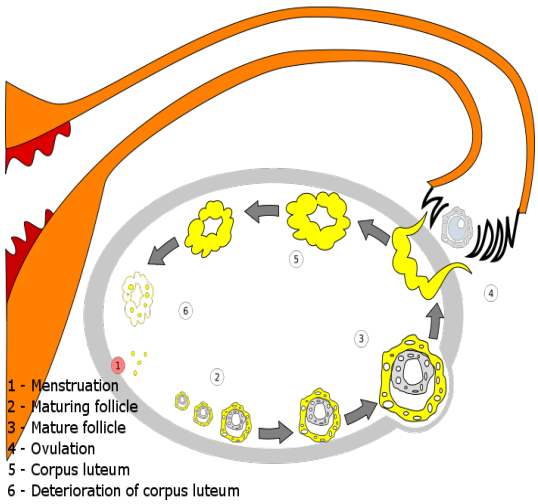

Figure 2.2: Folliculogenesis: Stages of an ovarian follicle [6]

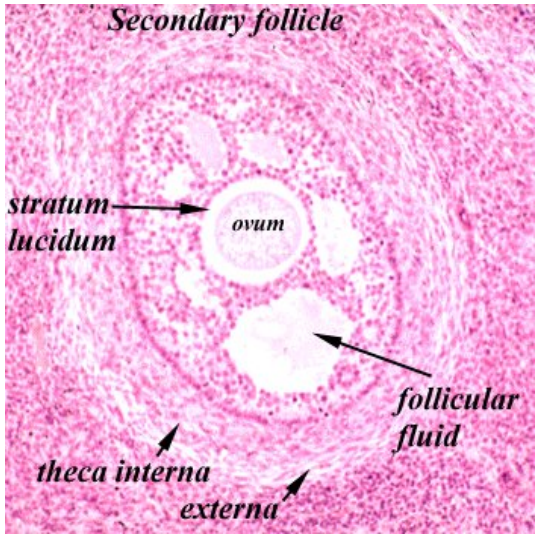

Figure 2.3: Human secondary follicle [7]

in the physiology of the hypothalmic-pituitary-ovarian axis which directs the ovarian cycle, intra-ovarian growth factors, fetal programming, metabolic consequences of insulin resistance, and heredity [14]. Of these theories, insulin resistance and the consequent metabolic syndrome X are gaining ground as the most probable hypotheses. Metabolic syndrome X is a cluster of risk factors associated with insulin resistance such as the overproduction of male hormones, elevated levels of blood fats, high blood sugar, obesity, hypertension, and ovarian dysfunction. Not all women with PCOS are diagnosed with insulin resistance; hence, there needs to be further research to establish the exact cause. The clinical phenotypes of patients diagnosed with PCOS fall under three categories:1) Oligo-ovulation+hyperandrogenism+hirsutism; 2) Oligo-ovulation+hyperandrogenism; and, 3) Oligo-ovulation+hirsutism, where oligo-ovulation means irregular ovulation, hyperandrogenism means excess male hormones, and hirsutism means male patterm hair growth [18]. The presence of such different clinical phenotypes among PCOS patients implies that the metabolic factors associated with the pathophysiology of PCOS could be varied indicating the variations in the clinical presentation of PCOS. Due to the various phenotypic exhibitions, the international consensus requires the presence of two of the following three criteria for the diagnosis of PCOS: 1) Oligo or anovulation; 2) biochemical and/or clinical signs of hyperandrogenism; and, 3) the presence of at least one polycystic ovary on ultrasonographic examination [1].

2.2.2 Morphology of the Polycystic Ovary: Manual measurement of external and internal features [1]

2.2.2.1 External features of PCO: Volume

The volume of each ovary is calculated by measuring the maximum diameter of the ovary in the three planes: 1) Longitudinal; 2) transverse; and, 3) anterposterior [1]. The ovarian volume is calculated using the formula of a prolate ellipsoid, which is given as $\frac{\pi}{6}\times$(maximal longitudinal$\times$ transverse$\times$ anteroposterior diameters). The ovarian volume was calculated using other formulae that based their calculations on giving different weights to the different planes such as $\frac{\pi}{6}\times AP^2\times TV$, or $\frac{\pi}{6}\times(\frac{T+L+A}{3})^3$, where $T=$ trans-

verse, $L =$ longitudinal, $A =$ anteroposterior, $AP =$ anteroposterior diameter, and $TV =$ transverse diameter. The consensus definition for a PCO includes an ovarian volume of $> 10cm^3$ calculated using the formula for the prolate ellipsoid. The consensus drew this conclusion based on a number of studies which reported the mean ovarian volume to be $> 10cm^3$ for PCOS controls. The consensus opinion also states that until more data are collected and validated, the formula for prolate ellipsoid should be used for computing the ovarian volume [1].

2.2.2.2 External features of PCO: Surface Area

Three different methods are proposed for computing the ovarian area in a 2D ultrasonographic image. In the first method, the ovarian area is computed using the formula for an ellipse: $\frac{\pi}{4} \times major\ axis \times minor\ axis$. In the second method, an ellipse is fitted to the ovary and the area is computed automatically using the ultrasound machine. The third method computes the area by outlining the ovary by hand with automatic detection of the outlined area.

2.2.2.3 Internal features of PCO

The follicle size and count are estimated after scanning the ovary in the longitudinal plane covering from the inner to the outer margin, and the follicle diameter is estimated as the mean of the diameters in the longitudinal, transverse and antero-posterior planes. The use of a follicle count of > 12 each measuring between $2-9$ mm diameter for the diagnosis of PCO morphology was based on a study by Jonard et al., 2003 [19]. A size range of $2-9$ mm has been suggested as the diameter of the follicles with PCO morphology because, it was found that hyperandrogenism might result in excessive early follicular growth upto $2-5$ mm but, the growth of these follicles is stunted when they reach a size of around $6-9$ mm.

The following list of PCO definitions is quoted from the international consensus definition [1].

1. The PCO should have at least one of the following: either 12 or more follicles measuring 2-9 mm in diameter or increased ovarian volume ($> 10\ cm^3$). If there is

evidence of a dominant follicle (>10 mm) or a corpus luteum, the scan should be repeated during the next cycle.

2. The subjective appearance of PCOs should not be substituted for this definition. The follicle distribution should be omitted as well as the increase in stromal echogenicity and/or volume. Although the latter is specific to polycystic ovary, it has been shown that measurement of the ovarian volume is a good surrogate for the quantification of the stroma in clinical practice.

3. Observation of just one ovary fitting this definition or a single occurrence of one of the above criteria is sufficient to conclude the existence of the PCO. If there is evidence of a dominant follicle (>10 mm) or corpus luteum, the scan should be repeated next cycle. The presence of an abnormal cyst or ovarian asymmetry, which may suggest a homogeneous cyst, necessitates further investigation.

4. This definition does not apply to women taking the oral contraceptive pill, as ovarian size is reduced, even though the "polycystic" appearance may persist.

5. A woman having PCO in the absence of an ovulation disorder or hyperandrogenism ('asymptomatic PCO') should not be considered as having PCOS, until more is known about the patient's condition.

6. In addition to its role in the definition of PCO, ultrasound is helpful to predict fertility outcome in patients with PCOS (response to clomiphene citrate, risk for ovarian hyperstimulation syndrome (OHSS), decision for in-vitro maturation of oocytes). It is recognized that the appearance of PCO may be seen in women undergoing ovarian stimulation for in vitro fertilization (IVF) in the absence of overt signs of PCOS. Ultrasound also provides the opportunity to screen for endometrial hyperplasia.

7. The following technical recommendations should be respected:

   (a) State-of-the-art equipment is required and should be operated by appropriately trained personnel. Whenever possible, the transvaginal approach should be preferred, particularly in obese patients.

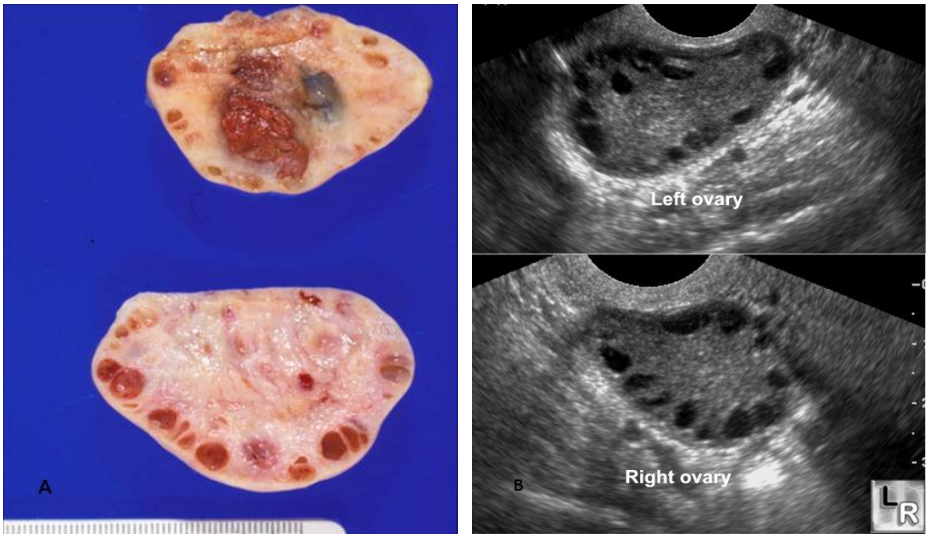

Figure 2.4: (A) Gross and (B) Ultrasonographic images representative of polycystic ovaries [8] [9]

(b) Regularly menstruating women should be scanned in the early follicular phase (days 3-5). Oligo-/amenorrhoeic women should be scanned either at random or between days 3-5 after a progestogen-induced bleed.

(c) If there is evidence of a dominant follicle (>10 mm) or a corpus luteum, the scan should be repeated the next cycle.

(d) Calculation of ovarian volume is performed using the simplified formula for a prolate ellipsoid ($0.5 \times length \times width \times thickness$).

(e) Follicle number should be estimated both in longitudinal, transverse and antero-posterior cross-sections of the ovaries. Follicle size should be expressed as the mean of the diameters measured in the three sections.

2.3 Ultrasonographic Imaging of Ovaries

Ultrasonographic imaging is a non-invasive imaging modality and is routinely used in scanning the uterus, ovaries, and the fetus because it is non-ionizing and inexpensive. This imaging technique is based on transmission of high frequency sound waves into the

body using a transducer and reconstructing the sound waves that are reflected off from the various organs. Reconstruction of the reflected sound waves as a two dimensional image is done based on calculating the depth of the tissue interface by measuring the time of return of the echo back to the transducer probe using the speed of sound in tissue and the time of the return of the echo [20] [21]. The intensity of a pixel on the reconstructed image depends on the strength of the echo. A strong echo is represented as a white pixel and a weak echo is represented as a black pixel and everything in between are represented by different shades of grey. A water based gel is applied on the surface of the skin before scanning to obtain good acoustic coupling, i.e., to lower the acoustic impedance mismatch between air and skin, where impedance is calculated as the product of the medium density and the velocity of the ultrasound beam in the medium. If no gel is applied, most of the transmitted sound waves will be reflected back because of the high impedance mismatch between air and skin [20] [21]. Energy reflected from an interface depends on the difference in acoustic impedance of the media on opposite sides of the interface. As water is a good transmitter of ultrasound and as the acoustic impedance of water is $\frac{1.5Kg}{m2s} * 10^{-4}$, which is close to the acoustic impedances of many organic substances, a better transmission coefficient is obtained when gel is applied before scanning [20] [21]. In Figure 2.4 the ovarian follicles appear as dark structures because the follicles are filled with fluid; as water is a good transmitter of ultrasound, most of the energy is transmitted and only a weak signal is reflected back to the transducer. There are two different ultrasonographic modalities available to image the female reproductive organs: trans-abdominal and trans-vaginal. Transrectal and tranlabial ultrasonographic modalities are also used rarely.

2.3.1 Artifacts

The common types of artifacts that occur in ultrasonographic imaging are reverberation, acoustic shadowing, acoustic enhancement, and refraction. Reverberation artifacts are caused by sound bouncing back and forth between two interfaces. Some of the sound returning to the transducer is reflected back to the patient. This pulse is hit again by the same interface and is reflected back to the transducer a second time. This type of artifact occurs mostly when the ultrasound pulse is perpendicular to a soft tissue - air

interface [20] [21].

Acoustic shadowing is caused by an imaged tissue whose rate of attenuation of sound is greater than that of the surrounding medium. This results in added loss of intensity when the pulse traverses through the tissue, making all points beyond the imaged tissue appear less brighter than expected. Acoustic enhancement is the opposite of acoustic shadowing, where the imaged tissue has a rate of attenuation of sound lower than the surrounding medium making all points beyond the tissue appear brighter than expected [20] [21].

Refraction artifact occurs when the ultrasound beam crosses tissues of different densities, which bends the beam due to the difference in velocity and the angle of incidence, creating a virtual object at a displaced position in the transducer [20] [21].

2.4 Stereology

It is important to derive the quantitative features of the follicles from the ovarian ultrasonographic images for making PCO diagnosis. It can be done manually or automatically using digital image analysis techniques. Computing two-dimensional features such as the diameter, perimeter, or the area on the two-dimensional ultrasonographic images can be done by counting the number of pixels in the given digital image, whereas computing the three-dimensional parameters is not as straight-forward. Three-dimensional attributes of a structure can be computed using methods such as 3D reconstruction, morphometry, and stereology. Of these, 3D reconstruction is complex and is mostly used for visualization purposes. Alternatively, stereology estimates 3D parameters of structures from the two-dimensional measurements that are obtainable on sections of the structure[22]. Stereological methods provide information on the dimensions of the spatial objects that make up a structure by studying its sections. Sections can be interpreted as projections of three-dimensional objects. Stereology has been used for studying the three-dimensional attributes of cellular structures and geological structures where test systems with known configuration are overlayed on top of these structures and the intersections of the structures with the points/grid lines are evaluated to derive the three-dimensional attributes of the unknown structures [22]. This methodology is well-suited for our application because

it allows direct estimation of the required three-dimensional follicle attributes. Some of the quantitative follicle features that are needed for the PCO diagnosis are the volume density and surface density of the follicles. Volume density is defined as the volume of the phase in the unit volume of the structure, where phase is defined as the aggregate of identical parts and surface density is defined as the surface area of the phase in the unit volume of the structure [22] .

2.4.1 Terminology of Stereology

The terminology followed by stereology has some unique definitions for some of the common terms like *structure*, *components*, *phase*, *objects or particles*, *density*, *section*, and *profile*. A structure is defined as a container with at least two parts or components, where a component is made up of either discrete units called objects or particles or occurs as a phase which is an aggregate of identical parts, such as the mitochondrial phase, where all the mitochondria of a cell constitute to the mitochondrial phase. A structure can be quantitatively described based on the density of the components within the structure. Hence, density of components in its varied forms becomes an important quantitative descriptor of the structure. Volume of the component phases, its surface area, length or the number of its particles play an important role in quantitatively describing the strucuture and are referred as the volume density, surface density, length density, and numerical density respectively. Density as a quantitative descriptor becomes important because sectioning is used as the sampling process, where sections are obtained by intersecting planes into the structure. The resulting images of the components or the structure within the section is termed a profile. Stereology establishes relationships between the density of the component profiles (within the structure profiles) and the density of the components (within the structure) by mathematical reasoning [22].

2.4.2 Stereological Principles

Stereological methods are based on geometric probabilities and are statistical in nature [22]. There are specific methods in stereology for making measurements of volume density, sur-

face density, length density, mean curvature density, numerical density, shape and mean tangent diameter of convex solids, profile size and particle size. Some of the more commonly used methods are the priniciple of Delesse, linear integration, the point counting method, intersections with test lines/profile boundaries and the Buffon priniciple. Volume density is measured using the Priniciple of Delesse, linear integration, and the point counting method. Surface density is measured using intersections with test lines/profile boundaries.

2.4.2.0.1 Volume density measurements[22] The principle of Delesse is based on the research of a French geologist who proved that the volume density of the various components making up a rock can be estimated by measuring their relative areas on the random sections, also called the areal density, of the profiles [22]. Principle of Delesse states that volume density of a component can be defined as the ratio of the sum of the object profile area (A_0) to the area of the object slide surface (A_T). This principle can be demonstrated by considering a model cube containing a tissue of one component spread out as evenly distributed irregular objects. The cube should be a part of a larger object so that the distribution of the tissue inside the cube should be consistent throughout down to the edges. Let the cube be placed in a *x,y,z*- coordinate system, parallel to the *x,z* plane and cut into slices of thickness dy. The area of the slide surfaces are given as a_T, where the area of the object profiles inside the section are given as a_0. The volume v_0 of these profiles can be calculated as $a_0 * dy$. The total volume of the slice is calcuated as $a_T * dy$. The volume density can be calculated by summing up the object volumes and the slice volumes of all the tissue slices and finding the ratio between them, which is given as:

$$\frac{\Sigma v_0}{\Sigma v_T} = \frac{V_0}{V_T} = V_v. \tag{2.1}$$

If the object volume and the slice volume are replaced with the product of its respective area and slice thickness, Equation 2.1 can be rewritten as:

$$\frac{\Sigma(a_0 * dy)}{\Sigma(a_T * dy)} = \frac{dy\Sigma a_0}{dy\Sigma a_T} = \frac{A_0}{A_T} = A_A. \tag{2.2}$$

Linear integration was proposed by Rosiwal for estimating A_A, which involves laying out test lines on the sections and measuring the fractional length of these lines included in

the profiles of the objects.

Point counting method for estimating volume density was proposed by Glagolev (1933) and Thomson (1930). This procedure was independently introduced by Chalkey (1943) in biology. In this method, a square grid is overlayed on top of a slice(structure), and the area of an object profile within the slice is determined by counting the number of squares that contain the object profile relative to the total number of squares on the section. For cases where an object profile occupies a square only partially, the decision to include or exclude the square for the area calculation depends on checking if at least half the square covers the object profile. If it does, the square is added in, else it is not. To make the area calculation simpler, the square grid can also be replaced with a grid of test points overlayed over the structure, where the number of test points covered by the object profiles relative to the total number of test points on the structure gives the areal density of the profile regions.

2.4.2.0.2 Surface density measurements[22] Surface density S_v is defined as the amount of surface area S_a contained in unit volume of tissue V_c. In stereology, surface density is estimated as $(4/\pi)\times$boundary density [22], where boundary density is the ratio of the length of profile boundary (B_a) to the section area of the ovary. The relationship between surface density and boundary density was derived by considering a model cube of side l containing a single sphere of radius R. A trace of the sphere taken by a plane section traversing the sphere will be a circle whose diameter depends on the distance of the plane section from the center of the sphere. The average radius of such circles produced by random sectioning is given as [22]:

$$\overline{r} = \frac{\pi}{4}R. \tag{2.3}$$

The average length of circle perimeter is given as:

$$\overline{b} = 2\pi\overline{r} = \frac{\pi^2}{2}R. \tag{2.4}$$

As the relative number of random sections that will hit the sphere depends on the ratio of the sphere diameter to the length of the cube ($\frac{2R}{l}$), the mean trace or the average circle perimeter of all the sections ($\overline{B}$) is given as:

$$\overline{B} = \overline{b}.\frac{2R}{l} = \frac{\pi^2 R^2}{l}. \tag{2.5}$$

With the section area (A_c) given as l^2, the mean boundary density ($\overline{B_A}$) is given as:

$$\overline{B_A} = \frac{B_a}{A_c} = \pi[\frac{\pi R^2}{l^3}]. \tag{2.6}$$

The surface density of the sphere (component) is given as the ratio of the surface area of the sphere (component) contained in unit volume of the cube (structure). Thus, surface density (S_v) of the sphere is given as:

$$S_v = \frac{4\pi R^2}{l^3}. \tag{2.7}$$

From Equation 2.7 it can be seen that, the term within square brackets in Equation 2.6 is $\frac{1}{4}$ of S_v. That is:

$$\overline{B_A} = \pi\frac{S_v}{4}. \tag{2.8}$$

or,

$$S_v = \frac{4}{\pi}\overline{B_A}. \tag{2.9}$$

Hence, it can be seen that the surface density of a component can be obtained from its boundary density.

CHAPTER 3

PREVIOUS WORK

This chapter gives a general overview of how ovarian ultrasonographic images are analyzed to study the tissue characteristics of ovaries or structures within it. Previous work in follicle segmentation and tissue characterization are discussed. The final section of this chapter discusses classifiers used for the classification of the tissue characterisitics or the features obtained from ovarian structures.

3.1 Follicle segmentation

The manual task of identifying the inner and the outer boundary of the follicle can be replaced with automated computerized approaches. Various follicle segmentation techniques have been proposed, and they can be categorized into grey-level thresholding and graph searching techniques [10], [23], region growing methods [2], texture-based methods [24] , object recognition algorithms [25], active contours or "snakes" [26], [27], and minimum cross entropy thresholding techniques [28]. Computer-aided diagnosis of prostate cancer with emphasis on ultrasound-based approaches are reviewed in [29]. The following sections review some of these techniques.

3.1.1 Graph searching

3.1.1.1 Semiautomated segmentation [10]

Sarty *et al.* [10] implemented a semiautomated segmentation method that identifies the outer boundary wall of a follicle using a knowledge-based graph searching algorithm. This method is based on using some *a priori* information available on follicle charac-

teristics. That is, follicles are fluid-filled structures and follicle fluid appears dark on an ultrasonographic image. Hence, the inner follicle wall that surrounds the fluid appear as a bright band around a dark region, whereas the outer follicle wall appears as a dark band that separates the follicle interior from the outside tissue. This *a priori* knowledge along with the knowledge that the follicle wall is of uniform thickness is used as the basis of this segmentation method that uses a graph searching technique to define the outer follicle border.

This method is divided into three main steps: 1) Defining an annular region of interest (AROI) to mark the follicle of interest; 2) detecting the approximate inner wall boundary of the follicle using Nilsson's graph searching algorithm with manual editing if needed; and, 3) automated detection of the outer follicle wall.

3.1.1.1.1 Defining AROI The follicle is defined using an annular region of interest, or AROI. An AROI has two concentric circles with the smaller circle completely inside the follicle-fluid and the larger circle completely enclosing the follicle. The diameters of the two circles are adjusted accordingly.

3.1.1.1.2 Detecting approximate inner boundary wall An edge sub image was constructed from the area inside the AROI using a 5 X 5 sobel-like edge operator with the following convolution masks:

$$h_1 = \begin{bmatrix} 64 & 64 & 0 & -64 & -64 \\ 64 & 64 & 0 & -64 & -64 \\ 127 & 127 & 0 & -127 & -127 \\ 64 & 64 & 0 & -64 & -64 \\ 64 & 64 & 0 & -64 & -64 \end{bmatrix} \tag{3.1}$$

$$h_2 = \begin{bmatrix} 64 & 64 & 127 & 64 & 64 \\ 64 & 64 & 127 & 64 & 64 \\ 0 & 0 & 0 & 0 & 0 \\ -64 & -64 & -127 & -64 & -64 \\ -64 & -64 & -127 & -64 & -64 \end{bmatrix} \tag{3.2}$$

and the edge magnitude of each pixel inside the subimage is calculated as: $M = \sqrt{x^2 + y^2}$, where x and y are the responses from h_1 and h_2 respectively. The area inside AROI is then resampled and the subimage is straightened out as a rectangular image with the inner circle of the AROI mapped to the top of the rectangle and the outer circle of the AROI mapped to the bottom of the rectangle. The edge direction, $d_I(k,i)$ for each pixel in the subimage was determined using a Prewitt operator, where k is the angular coordinate and i is the radial coordinate. This subimage is the *2D inner border detection graph* that is searched to find the approximate inner follicle boundary wall. The inner wall is found by finding the minimum cost path through the graph. The node costs are determined by first finding the edge pattern strength $P_I(k,i)$ of each node as follows:

$$P_I(k,i) = \begin{cases} f_I(k,i) & \text{for} \quad d_I(k,i) \in \{-\pi/4, 0, \pi/4\} \\ f_I(k,i) - dp & \text{otherwise,} \end{cases} \tag{3.3}$$

where dp is the directional penalty applied to nodes that do not favor the preferred edge direction, where the preferred edge direction is dark to bright edges when viewed from inside the AROI. The node cost is given as:

$$c_I(k,i) = \max_{y \in Y} \{P_I(k,i)\} - P_I(k,i). \tag{3.4}$$

where Y is the width of the straightened edge subimage. Here, assignment of node costs are based on the *a priori* knowledge that the follicle-fluid appears dark. Once, the node costs are assigned, Nilsson's graph searching algorithm is applied to the edge subimage, which gives the optimal inner border. At this stage, there is an interactive correction of the inner border wall if there are any variations.

3.1.1.1.3 Detecting the outer follicle wall Once the approximate inner follicle border wall is estimated, the edge subimage is again resampled and straightened out with new dimensions based on the newly estimated approximate inner border. The new region of interest (ROI), is moved by 1.4 mm inward, in the direction perpendicular to the inner wall border, and is the inside limit of ROI. The outer limit of ROI is estimated by moving the inside limit of ROI by 4.2 mm outward. This dimension was chosen to make sure that the outer and the inner border wall lies within the ROI. This resampled edge image is

used as the *outer border detection graph*, and the new edge intensities $f_O(k,i)$ and edge directions $d_O(k,i)$ are calculated. The node costs in the outer border detection graph are determined using the revised edge pattern strengths, which depend on the following local edge functions:

$$f_{BW}(k,i) = \begin{cases} f_O(k,i) & \text{for} \quad d_O(k,i) \in \{-\pi/4, 0, \pi/4\} \\ f_O(k,i) - dp & \text{otherwise,} \end{cases} \tag{3.5}$$

$$f_{WB}(k,i) = \begin{cases} f_O(k,i) & \text{for} \quad d_O(k,i) \in \{3\pi/4, \pi, -3\pi/4\} \\ f_O(k,i) - dp & \text{otherwise,} \end{cases} \tag{3.6}$$

where, f_{BW} favors an edge direction from black to white and f_{WB} favors white to back, when viewed from inside the ROI. Unlike in the approximate inner wall border detection where edge strength of a node depends upon just its edge intensity and direction (local edge strength), in outer wall border detection the edge strength of a node is also affected by the nearby edge strengths coming from the inner wall border ($e_i(k,i)$), and the inner/outer wall border of the nearby follicles ($e_o(k,i)$) (Figure 3.1). Hence, the edge pattern strength $P_O(k,i)$, is given as a weighted sum of its local edge strength, $e_i(k,i)$, and $e_o(k,i)$:

$$P_O(k,i) = W_0 f_{WB}(k,i) + W_1 e_i(k,i) + W_2 e_0(k,i), \tag{3.7}$$

where

$$e_i(k,i) = \max_{y \in \{-6,\ldots,-2\}} \{f_{BW}(k, i+y)\}, \tag{3.8}$$

$$e_o(k,i) = \max_{y \in \{2,\ldots,10\}} \{f_{BW}(k, i+y)\}. \tag{3.9}$$

The node cost function was assigned as:

$$c_O(k,i) = \max_{y \in Y} \{P_O(k,y)\} - P_O(k,i), \tag{3.10}$$

where, Y represents the width of the straightened subimage. The inner wall border served as the shape model for the outer wall border detection and it corresponded to a straight line in the outer wall border detection graph. Hence, any deviations from the straight line were assigned a penalty mp, to the node cost $c_O(k,i)$. The node cost $c_O(k,i)$ is further

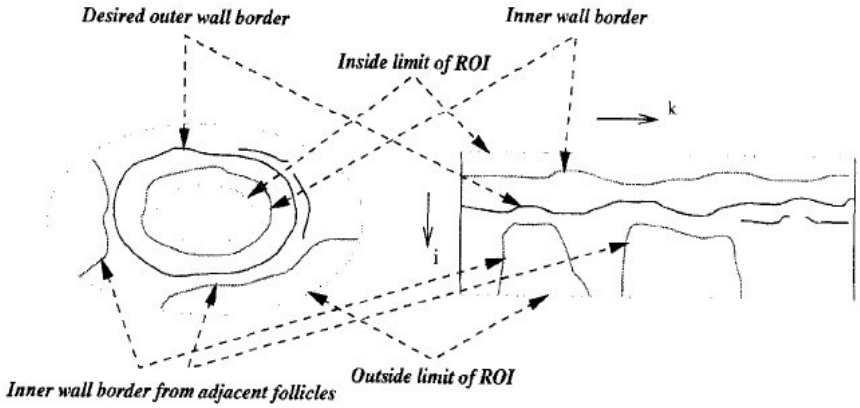

Figure 3.1: Location of the edges that affects the cost function. [10].

revised by taking into account the direction from which the node (k,i) was reached from its predecessor $(k-1,j)$ and is given as:

$$C_{model}(k,i) = \begin{cases} c_O(k,i) & \text{if} \quad predecessor \quad border \quad node \quad j=i \\ c_O(k,i)+mp & \text{otherwise,} \end{cases} \tag{3.11}$$

The outer follicle wall is determined by searching the outer border detection graph with the new nodal costs, $C_{model}(k,i)$ and are mapped back into the original image.

3.1.1.2 Automated segmentation [23]

The fully automated follicle segmentation method of Krivanek and Sonka [23] follows a four step process: 1) Watershed segmentation to isolate the antrum (follicle-fluid interior) to find the approximate inner border; 2) selection of the follicle of interest; 3) inner border detection; and, 4) finally outer border detection using Nilsson's graph searching technique.

3.1.1.2.1 Watershed segmentation The process of finding the approximate inner border is further divided into four stages: 1) Preprocessing the original image; 2) watershed segmentation of grayscale image; 3) watershed segmentation of binary image; and, 4) postprocessing to get rid of false separations.

3.1.1.2.1.1 Preprocessing A subimage is obtained from the original 640×480 input image and is smoothed twice using adaptive neighborhood smoothing method. Deter-

mination of the threshold is experimentally determined relatively easily since the antrum (interior) of the follicle is dark and will consistently have lower intensities than the chosen threshold T.

3.1.1.2.1.2 Watershed segmentation of grayscale image A watershed algorithm segments an image similar to how crestlines isolate catchment basins of topographical surfaces. That is, if we imagine poking holes in regions of minima in the given image and immersing it in water, watershed lines are built at locations where two catchment basins would merge as a result of further immersion. The iterative immersion watershed algorithm of Vincent and Soille [30] is used to perform watershed segmentation of the grayscale smoothed subimage. This method first sorts the pixels in the increasing order of the grayscale intensities and then performs a breadth-first search flooding. Watershed segmentation results in over-segmentation if there is noise and local irregularities in the gradient image, hence the segmented image is processed further to resolve the problem of over-segmentation. A mosaic image is constructed from the labelled image of watershed transformation by assigning the average of the pixels of each labelled region from the smoothed image to each labelled region and thresholding the resulting mosaic image. This image is processed further to separate the connected follicles.

3.1.1.2.1.3 Watershed segmentation of binary image A morphology image (image that is constructed by applying morphological operators) is constructed from the binary image of the previous step by removing small objects, separating out overlaps of smaller objects, and correcting sporadic variations along the object edges. Then, the inverse Euclidean distance map (EDM) is calculated for the morphology image, where the distance of each pixel to its boundary is mapped as the brightness level of a pixel in the EDM. Finally, watershed segmentation is applied to this image.

3.1.1.2.1.4 Post-processing This step is performed to distinguish correct and incorrect region splitting, by merging false separations that results from applying watershed transformation to the smoothed morphology image. This is done by first calculating the border length, average edge strength, and average gray level along the boundary in an

eight-connected neighborhood. The subregions are merged based on the following algorithm:

1: **if** $ES_b > ES_{thresh}$ **then**
2: Split
3: **else**
4: **if** $B_l > R_{mA}$ **then**
5: Merge
6: **else**
7: **if** $AG_b < B_{thresh}$ **then**
8: Merge
9: **else**
10: **if** $ES_b < ES_{thresh}$ **then**
11: Merge
12: **else**
13: Split
14: **end if**
15: **end if**
16: **end if**
17: **end if**

where ES_b is the edge strength along the boundary; ES_{thresh} is the edge strength threshold; B_l is the boundary length between two subregions; R_{mA} is the ratio of the minor axis; AG_b is the average gray level along the boundary; and B_{thresh} is the brightness threshold. So, if a common boundary defines a strong edge, then the subregions are split.

3.1.1.2.2 Identification of follicle of interest This is the only interactive step of this otherwise fully automated method. The user points to the follicle of interest using a mouse. As the antrum (follicle interior) of all the follicles has been already determined using the watershed transformation method, pointing the mouse over the follicle of interest gives the screen coordinates of the mouse click that automatically chooses the correct subimage that should be processed further to determine the exact inner and outer boundary wall. Thus,

the region of interest (ROI) is found automatically.

3.1.1.2.3 Inner wall detection The inner and the outer limits of the inner border region of interest (IROI) are found by scaling the marked follicle to 80% of its original size, which gives the inner limit, and then moving 30 pixels outward from the inner limit, which gives the outer limit of IROI. Edge intensity, edge direction, edge pattern strength, and nodal costs for IROI are the same as the previous technique. To find the exact inner border, the nodal costs are further modified that takes into account the direction from which the node (k,i) was reached from its predecessor $(k-1,j)$, and applies a penalty mp, if node (k,i) was reached from $(k-1,j)$ when $j \neq i$. The optimal path through this graph gives the inner wall border.

3.1.1.2.4 Outer wall detection The outer wall border can be defined from the inner wall border. The inner limit of the outer border region of interest (OROI) is found by moving 1.4 *mm* inwards from the already detected inner border, and the outer limit of OROI is found by moving 2.8 *mm* outwards from the detected inner border. Once the inner and outer limits of OROI is determined, the edge pattern strengths, nodal costs, and revised nodal costs of the subimage are computed. The optimal path through OROI gives the outer border wall of the follicle of interest.

3.1.2 Follicle segmentation with region growing [2]

The region growing method of Potočnik and Zazula[2] is based on considering the follicles as homogeneous dark regions on which region growing is performed. This method is a fully automated algorithm requiring no human intervention at any stage unlike the previously discussed segmentation methods. It is composed of three main steps: 1) Identification of the homogeneous regions; 2) growing the homogeneous regions until they reach the inner border wall; and, 3) finally extracting the follicle from the grown regions. The automatic segmentation of follicles in our system was done using a modified version of this algorithm and is explained in detail in Chapter 4.

3.2 Analysis of normal and PCOS ovaries

The other important application of processing ultrasonographic images is to distinguish between normal and abnormal ovaries. That is, ovarian ultrasound is also used for detecting abnormalities such as ovarian cancer, and ovarian cysts (which is an indication of ovarian tumor), although the image speckle of ultrasonographic images makes it difficult to process the image for such abnormalities.

The texture-based segmentation of Jiang and Chen [3] uses a texture-based pixel classifier based on four texture energy measures to distinguish between normal and abnormal ovaries for the detection of ovarian cancer. Zimmer *et al.* [4] have presented a semiautomatic way for quantification of ovarian cysts.

3.2.1 Texture-based pixel classifier [3]

Texture-based k-means cluster analysis [3] does not use the standard intensity-direction edge information for segmentation, because tissue edges are blurred in ultrasonographic images and is also indistinct because of speckle noise. This texture-based pixel classifier reevaluates the original Laws' feature masks and derives new texture features to be applied to the k-means clustering as it has been found that the original feature masks does not give satisfactory results on ultrasonographic images.

Laws' texture feature masks representing different operations are derived by convolution of three basic vectors L_3 = (1, 2, 1), E_3 = (-1, 0, 1), and S_3 = (-1, 2, -1), which represents one-dimensional center-weighted local averaging, first differencing for edge detection, and second differencing for spot detection respectively. These vectors can be convolved with themselves or with one another to give five vectors: averaging filter L_5 = (1, 4, 6, 4, 1), edge detector E_5 = (-1, -2, 0, 2, 1), spot detector S_5 = (-1, 0, 2, 0, -1), ripple detector R_5 = (1, -4, 6, -4, 1), and wave detector W_5 = (-1, 2, 0, -2, 1). These five vectors give 25 5×5 feature masks, which is obtained for example by multiplying a column vector L_5 with a row vector E_5 that gives a 5×5 feature mask, and repeat this for each of the five vectors which would give 25 5×5 feature masks. The feature masks can extract 25 patterns by convolving with an image with different textures. However, Jiang and Chen

showed that a clear pattern of texture features can be extracted from ultrasonographic images using just four masks $L_5 * E_5$, $S_5 * E_5$, $E_5 * L_5$, and $E_5 * E_5$ (Figure 3.2). The original

$$\begin{vmatrix} -1 & -2 & 0 & 2 & 1 \\ -4 & -8 & 0 & 8 & 4 \\ -6 & -12 & 0 & 12 & 6 \\ -4 & -8 & 0 & 8 & 4 \\ -1 & -2 & 0 & 2 & 1 \end{vmatrix} \quad \begin{vmatrix} -1 & -4 & -6 & -4 & -1 \\ 0 & 0 & 0 & 0 & 0 \\ 2 & 8 & 12 & 8 & 2 \\ 0 & 0 & 0 & 0 & 0 \\ -1 & -4 & -6 & -4 & -1 \end{vmatrix}$$

$$\begin{vmatrix} -1 & -4 & -6 & -4 & -1 \\ -2 & -8 & -12 & -8 & -2 \\ 0 & 0 & 0 & 0 & 0 \\ 2 & 8 & 12 & 8 & 2 \\ 1 & 4 & 6 & 4 & 1 \end{vmatrix} \quad \begin{vmatrix} 1 & 2 & 0 & -2 & -1 \\ 2 & 4 & 0 & -4 & -2 \\ 0 & 0 & 0 & 0 & 0 \\ -2 & -4 & 0 & 4 & 2 \\ -1 & -2 & 0 & 2 & 1 \end{vmatrix}$$

Figure 3.2: Feature masks [3].

image is convolved with the four feature masks to give the feature image $g(i, j)$, from which the mean and deviation around each pixel is calculated as follows:

$$s[i, j] = \frac{1}{(2n+1)^2} \sum_{k=i-n}^{i+n} \sum_{l=i-n}^{i+n} |g[k, l] - mean| \tag{3.12}$$

where,

$$mean = \frac{1}{MN} \sum_{ij} g[i, j], \tag{3.13}$$

and $s[i, j]$ forms the four-dimensional feature space for the k-means clustering process that divides each pixel in the image as one of the following three groups: 1) Non-ovarian tissue; 2) normal ovarian tissue; and 3) abnormal ovarian tissue. This is done by selecting three seed points from three feature vectors that are centers of three regions in feature space. It takes the current seed points, classifies them based on the minimum Euclidean distance between the seed points and the feature vectors. Once a seed point belongs to a particular class, the seed points are recalculated as the mean of the pixels in the class. This process is repeated until the shift in the means becomes less than a preset value. This method achieves a good segmentation of normal and abnormal ovarian tissues.

3.2.2 Semiautomatic algorithm for quantification of ovarian cysts by Zimmer *et al.* [4]

The morphological characteristics of an ovarian cyst include its size, regularity and thickness of its boundary, fluid characteristics, and the presence of structures such as papillations and septations. Papillations are structures that grow from inside the boundary of a cyst towards its lumen or the inner membrane space. They are incomplete and do not divide the cyst into separate regions (unilocular). A septation is long and divides the cyst into separate regions (multilocular). The algorithm of Zimmer *et al.* does a morphological classification of these structures to determine the malignancy of the ovarian pathology, using scoring systems and a minimum error rate Bayesian classifier. That is, the quantified properties of these cystic structures are scored according to a predetermined table and the resulting values are used for classification.

This method starts by separating the cysts from the background as the cysts appear as dark regions in ultrasound B-scans. Next, convex hulls of the cysts are determined to calculate the convex deficiency of the cyst. Convex deficiency is obtained by subtracting the original cyst from its convex hull. This value gives an indication of the upper limit of the area of the cystic structures. Then a new image is formed by applying a morphological closing using a binary disk on the original cyst. This results in closing the convex deficiency indicative of the cystic structures, but which leaves a crater in the outer part of the concavities. Binary disks of different radii are applied and the minimal radius that covers at least 50% of the convex deficiency is chosen. If the disks fill only a small part of the convex deficiency leading to the underestimation of the cystic structures, then the convex deficiency is used for describing the cystic structures, instead of the result of the morphological closing. There can be an underestimation of the cystic structures when morphological closing is applied as can be seen in Figure 3.3(*b*). This can be corrected by taking the regions for which the morphological closing was applied and replacing them with their convex hulls (Figure 3.3(*c*).

Figure 3.3(*a*) shows the initial convex deficiency, 3.3(*b*) shows the result of morphological closing using a binary disk, and 3.3(*c*) shows the structures on which the

morphological closing was applied replaced with its convex hull.

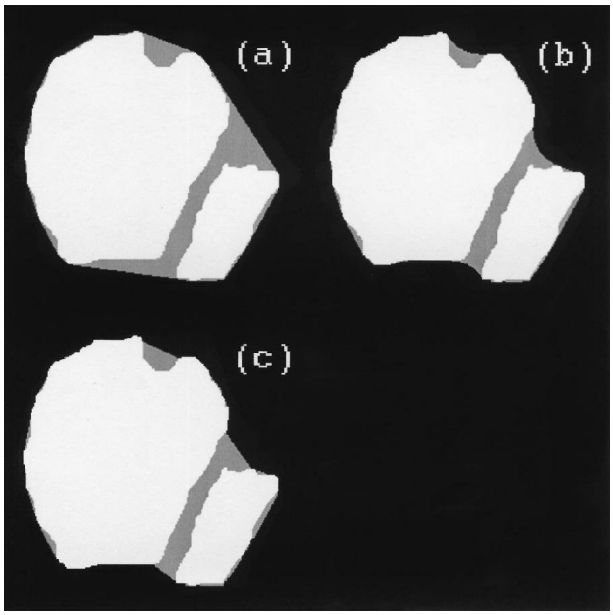

Figure 3.3: In this figure, the original cyst is white and the convex deficiency is gray. (a) Initial convex deficiency obtained by subtracting the original cyst from the convex hull (b) Convex deficiency after morphological closing (c) Corrected convex deficiency after replacing figure (b) with the convex hull [4].

The shape features for the classification were chosen to be the area, roundness of the shape (compactness), and a value specifying what percentage of the cystic structure touches the cyst boundary (white region in Figure 3.3). The last measure is called the "pop" and it is given as:

$$pop = 100 * \frac{length\_of\_portion\_touching\_cyst}{total\_length\_of\_perimeter}. \tag{3.14}$$

This value is an indication of the kind of structure present inside the cyst. For example, a value of pop between 75%-95% represents that it is a septation, a value between 60%-80% means it is a papillation, and a value of 50%-60% indicates it is a side structure meaning that it would not be used in the quantification. Also, structures that have an area less than 1% of the area of the cyst are categorized as false structures and are removed. The available data for a specific shape are described as a feature vector in a two-dimensional feature space. Then this shape belongs to class k, if it gives a minimal value for the

equation over all classes:

$$F_k = (x-\mu_k)^t \sum_k^{-1} (x-\mu_k) + ln(|\sum_k|) \tag{3.15}$$

where, k = 1, 2, 3, μ_k is the mean vector of class k, and $\sum_k$ is the covariance matrix of class k. The mean vector and the covariance matrix of class k are found using a training sample set. Then the classification technique was applied to a test group of unidentified shapes using the obtained values. Once the structures are identified using the Bayes classifier, the quantitative data is extracted using morphological erosions (Appendix 2 of [4]). The final classifications were compared with that of a human expert in the field. This technique achieved correct classification rates of 72.3% for the papillations (34 out of 47 cases), 75% for the septations (12 out of 16 cases), and 90.2% for the side structures (37 out of 41 cases) [4].

3.3 Classifiers

The tissue characterisitics or the features obtained from the ovarian structures are classified using classifiers such as the linear discriminant classifier, k-nearest neighbor classifier (`knnclassify` in Matlab R2006a), and the Support Vector Machine Classifier (function `svmclassify` in Matlab R2006a). The two former implementations are part of Matlab's statistics toolbox, and the latter is from Matlab's Bioinformatics toolbox.

3.3.1 Linear discriminant

The method of linear discriminant analysis was originally developed by R.A. Fisher in 1936 and is a classic method used for categorical classification. The basic idea of this method is to classify two or more categories(groups) with n variables by projecting the high dimensional data onto a line and performing classification in this one-dimensional space. If for example there are two groups (classes) involved, the projection should maximize the distance between the mean of these two groups (between-class variance), and minimize the within-class variance of each group (variance within each class). For all

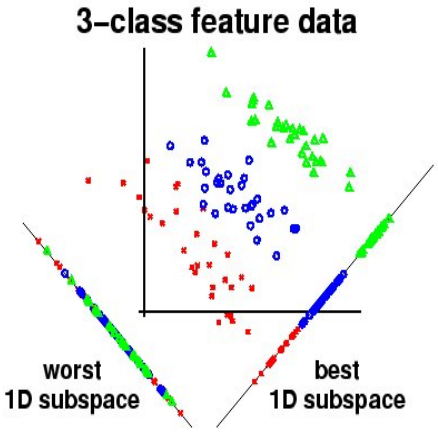

Figure 3.4: LDA: 3-class feature data projected on two rotated axes[11]

linear projections w, the following measure $J(w)$ should be maximized as per the Fisher criterion [31].

$$J(w) = \frac{|m_1 - m_2|^2}{s_1^2 + s_2^2} \tag{3.16}$$

where m_1 and m_2 are the means of $class1$ and $class2$, and s_1 and s_2 are the variance of $class1$ and $class2$. The projection seeks to rotate the axes so that the when classes are projected onto this axes the differences between the classes are maximized. In Figure 3.3.1, the projection of the categories to the lower left axes gives the worst separation of the classes, and the projection to the lower right axes gives the best separation of the classes.

3.3.2 KNN K-Nearest Neighbor Classification

K-nearest neighbor algorithm is one of the simplest machine learning algorithms. In this algorithm, an unknown feature (test dataset/pattern) is classified as belonging to the class to which the majority of its K closest training neighbors in the feature space belong. First, all the training datasets/patterns represented as feature vectors are positioned on a multi-dimensional feature space. Then, the distance between the unknown feature (test feature) and the training feature vectors is computed using a distance metric such as the Euclidean distance to choose the K- nearest neighbors of the unknown feature. If the value of K is

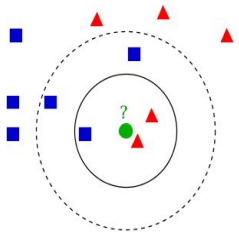

Figure 3.5: KNN: Distribution of the training vectors on a feature space

chosen as one, it is called the nearest-neighbor algorithm. The optimal value of K can be determined using cross-validation technique. To eliminate situations of tie, K can be chosen as an odd number. Once the K-nearest neighbors are found, the class of each of those neighbors is determined and the unknown feature is assigned to the class to which majority of its K neighbors belong. This algorithm might become computationally expensive if the training dataset is large as the Euclidean distance must be computed for every vector in the feature space. The performance of this algorithm is also limited when there is more noise in the training dataset as it might introduce bias during classification, especially when K is chosen as a small integer.

Figure 3.5 shows the distribution of the training vectors on a feature space [32]. The unknown vector (green dot) is classfied to the class of red triangles if $K = 2$, but would be classfied to the class of blue squares if $K = 3$. It would still be classified to the class of blue squares if $K = 5$ (3 nearest blue squares versus 2 nearest red triangles). This classification was implemented using the *knnclassify* function of Matlab R2006a.

3.3.3 Support Vector Machine Classification

The SVM classifier tries to build a maximum-margin separating hyperplane that maximizes the distance between two parallel hyperplanes that separate the data. The vectors that lie on the two parallel hyperplanes are called the support vectors. Mostly, all linear classifiers are based on the idea of building a hyperplane to separate the two sets of data and the difference between the SVM classifier and the other linear classifiers is that the SVM classifier tries to maximize the distance between the two parallel hyperplanes to

minimize the generalization error. The dividing hyperplane takes the form

$$w \cdot x - b = 0, \tag{3.17}$$

where w is normal to the dividing hyperplane and the offset b allows to increase the margin without which the hyperplane would pass through the origin.The two parallel hyperplanes are described as

$$w \cdot x - b = 1 \tag{3.18}$$

$$w \cdot x - b = -1, \tag{3.19}$$

where 1 or -1 is the constant denoting the class to which the point x_i belongs to, where x_i is a p-dimensional vector. Using geometry, it is found that the distance between the two parallel hyperplanes is given as $\frac{2}{|w|}$. So, to maximize the distance between the two parallel hyperplances, $|w|$ has to be minimized. Data points can be excluded by ensuring for each i Equation 3.20 is followed. Figure 3.6 [12] shows the dividing hyperplane, support vectors, and the two parallel hyperplanes.

$$w \cdot x_i - b \geq 1 \text{or} \tag{3.20}$$

$$w \cdot x_i - b \leq -1 \tag{3.21}$$

Equation 3.20 can be rewritten as

$$c_i(w \cdot x_i - b) \geq 1, 1 \leq i \leq n \tag{3.22}$$

where c_i is a contant 1 or -1 representing the class of x_i, and n is the number of training patterns used to train the classifier. Thus, the primal form is to minimize $|w|$ subject to the constraint Equation 3.22. This is a Quadratic programming (QP) optimization problem.

For non-linear classification, the kernal trick is applied to the separating or the maximum-margin hyperplanes. The kernel trick transforms the non-linear observations to a higher dimensional space where the linear classfier would be subsequently applied. So, this makes the linear classfication in the new space a non-linear classification in the original space. Thus, in the resulting algorithm each dot product of the linear classifier is replaced with a non-linear kernel function to make the maximum margin hyperplane fit in the transformed

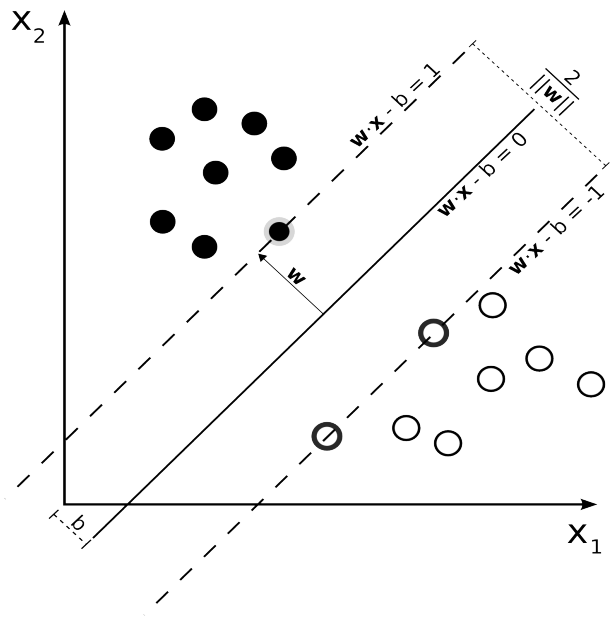

Figure 3.6: Maximum-margin hyperplane and margins for a SVM trained with samples from two classes. Support vectors lie on lines w.x - b=1 and w.x - b=-1 [12].

feature space. Some of the non-linear kernels used are polynomial, radial basis function, and sigmoid functions.

In Matlab, the SVM classifier is first trained using function *svmtrain* that accepts as input the rows of training data and a column vector of the class information for each row of training data. Each row in the training data is an observation and each column is a feature. The default setting of the *svmtrain* function is the linear kernel or dot product which was also used for our training dataset. The information about the trained SVM classifier is returned in a structure *SVMStruct* that has the following fields: SupportVectors; Alpha, Bias; KernelFunction; KernelFunctionArgs; GroupNames; SupportVectorIndices; ScaleData; and, FigureHandles. This structure can now be used to classify the test data using *svmclassify*, which accepts as its input the structure (*SVMStruct*) and the test data. The return value of *svmclassify* indicates the class to which each row of test data has been assigned to. The performance of the classifier can be analyzed using Matlab function *classperf*.

3.3.4 Validation

Once a classifier model has been learned from the training patterns, its ability to classify new patterns can be assessed using cross validation techniques. This is accomplished by using only part of the available patterns for training. The remaining "test" data are used to test the performance of the learned model. Common types of cross validation methods are the holdout method, and the k-fold cross validation method [33].

In the holdout (or half-and-half) method, the data set is randomly split into a training set and a testing set. A model is learned from the training set and the validity of the model checked by determining the classification accuracy of the model using the testing set. Model accuracy is dependent on the particular split of the data. The disadvantage of the holdout method can be avoided by using the k-fold cross validation technique. In this method, the data set is divided into k folds, out of which $k-1$ folds are used as the training set, and the remaining fold is used as the testing set. The holdout method is performed k times, each using a different fold as the testing set thus eliminating the dependence on the division of the data points among the training and the testing sets. The classification accuracy is averaged over the k trials and the variance decreases as k increases.

CHAPTER 4

METHODOLOGY

The automatic detection of polycystic ovary morphology involves three steps: 1) Segmentation of follicles from the ultrasonographic images; 2) application of stereological methods on the segmented follicles to derive their quantitative features; and 3) finally classification of the derived follicle features as polycystic or normal.

The region growing method of Potočnik and Zazula [2] was chosen for follicle segmentation due to its fully automatic nature. The regions corresponding to the ovaries were manually segmented from the ultrasound images first before being input to this algorithm. In tests of this method, the recognition rate of follicles was approximately 78% with a misidentification rate of 29%(std 25%) [2].

4.1 Follicle Segmentation

The region growing algorithm of Potočnik and Zazula [2] operates in three phases: 1) identification of homogeneous regions; 2) region growing; and 3) follicle extraction. Since this algorithm was designed to segment follicles in normal ovaries, some modifications were made in order to segment polycystic ovaries. Subsections 4.1.1 through 4.1.3 detail the algorithm; modifications from the original version [2] are noted.

4.1.1 Identification of Homogeneous Regions

A homogeneous region was considered to be one in which the pixels had similar greyscale values. Identification of homogeneous regions was achieved by filtering the image with an adaptive neighborhood median filter using a threshold T_1, which was set to the mean grey level of the original image. Pixels with intensity below T_1 were filtered using an

11×11 neighborhood, and pixels with intensity above this threshold were filtered using a 5×5 neighborhood. This causes a greater amount of smoothing in darker regions which are more likely to be part of a follicle and better preserves edges in brighter regions. The smoothing step was then repeated to ensure elegant smoothing of follicle regions. An 11×11 neighborhood size was chosen because a distance of 50 to 60 pixels in an ovarian ultrasonographic image corresponds to approximately 10 mm in reality. This size ensured that follicle interior regions were smoothed more thoroughly than the follicle edges or the high intensity regions. Since this step was part of the coarse estimation of follicle regions, highly accurate determination of the threshold T_1 was not paramount. The filtered image was then thresholded using a new rough threshold, T_2, which was set to the mean intensity of the smoothed image minus one standard deviation of pixel intensities in the smoothed image. Structures which were incorrectly merged using this procedure were coarsely separated using binary watershed segmentation. The above procedure resulted in some undesired homogeneous regions that were too small to be follicle regions. Such regions were removed by deleting regions whose area in pixels fell below a threshold of T_3. T_3 was set to 50, which is approximately a quarter of the area of the minimum detectable follicle size. The identified homogeneous regions were then sorted in descending order by area and passed on to the region growing step.

4.1.2 Region growing

The homogeneous regions from the previous phase are intial approximations of the follicles. The approximation typically underestimates follicle area and results in regions roughly centered within the actual follicle region. It is therefore appropriate to use region growing to expand the regions to the actual follicle boundary.

Each homogeneous region was grown using an iterative process in which an individual pixel is marked as a potential candidate for merging with a homogeneous region if it satisfied two merging criteria. The first criterion (Equation 4.1) is based on the intensity of an individual pixel; the second criterion (Equation 4.3) is based on weighted gradients.

Let R_0 be the initial homogeneous region prior to being grown. Region growing proceeds iteratively. Let R_i denote the resulting region after i iterations of region growing.

Let $p_0 ... p_n$ be the pixels from the outer boundary of region R_i. For each iteration, Equations 4.1 and 4.3 were evaluated for all pixels $p_0 ... p_n$ in the outer boundary. Pixels that satisfied both criteria were marked as potential candidates for merging with R_i to form R_{i+1}. The first criterion was:

$$|I(p_i) - m(R_i)| \leq \alpha\sigma(R_i), \tag{4.1}$$

where, $I(p_i)$ is the intensity of pixel p_i, $m(R_i)$ is the mean grey-level of region R_i, and $\sigma(R_i)$ is the standard deviation of grey-levels for pixels in R_i. The scaling parameter, α, was chosen to be 1.

The second criterion used edge and texture information. Edges can be detected by computing the gradient of the image. However, since region boundaries are not well expressed in ultrasonographic images, a weighted gradient was used. The weighted gradient magnitude is:

$$grad(p_i) = ||\nabla I_k(p_i)||(e^{G/tex(p_i)} - 1), \tag{4.2}$$

where $||\nabla I_k(p_i)||$ is the gradient magnitude of I_k, $tex(p_i)$ is the ratio of the mean grey-level and one standard deviation of grey-levels in the 11×11 neighborhood about pixel p_i, and $G = 2\ln(2)$. As $tex(p_i) \to \infty$, the exponential approaches 0, and when $tex(p_i) = 1.91$, exponential quantity is 1. The value 1.91 is the average signal-to-noise ratio (SNR) in regions with ultrasound speckle. Hence, $grad(p_i)$ is small for anechogenic follicle regions in which there is no speckle and large for edges and noisy regions. The second merging criterion was given as:

$$|grad(p_i) - m(grad(R_i))| \leq \alpha\sigma(grad(R_i)), \tag{4.3}$$

where, $m(grad(R_i))$ is the mean weighted gradient and $\sigma(grad(R_i))$ is the standard deviation of the weighted gradient in region R_i. The scale factor α was set to 2 [2].

In the original method, the marked potential candidates were merged with the homogeneous region if at least four of their neighbors were either in R_i already, or had also been marked as potential candidates. In our method, two new criteria have been added in addition to the above two merging criteria. Marked potential candidates are merged with the homogeneous regions based on the values of two region-based scalar descriptors:

solidity and eccentricity. Solidity is the proportion of the pixels in the convex hull of a region that are also in the region, and eccentricity is the ratio of the lengths of the major and minor axes of a region. If the solidity of the merged region (original region merged with a potential candidate), is less than the original region, then the potential candidate is unmarked. Also, if eccentricity of the merged region is greater than the original region, or if it is greater than a threshold T_4 which is set as 0.72, then the potential candidate is unmarked. An eccentricity of 1 corresponds to a circular shape, and it was found that an eccentricity of 0.72 gave optimum results for segmentation of follicular structures. These shape descriptors are an important addition to the merging criteria as they ensure that regions retain a compact shape during growth. The growing was halted when the final region R_n was equal to that of the previous step R_{n-1}.

4.1.3 Follicle extraction

The identified regions of the previous step were further analyzed in an attempt to remove those that did not correspond to an actual follicle. Identified regions with an area less than 220 pixels were removed since this corresponds to the approximate area of the smallest visible follicles (2 to 3 mm diameter). Also, if the ratio of a follicle's area to that of the area of its bounding box was less than 0.5, it was removed from consideration. All the regions satisfying these two measures were labelled and holes inside them filled.

4.2 Stereology and Feature Extraction

The second phase of the polycystic ovary detection algorithm is the generation of a feature vector for the segmented (labelled) follicles in a given image. These feature vectors are used in the third phase of the algorithm (see Section 4.3) which classifies feature vectors as either from polycystic or normal ovaries.

Features were derived using a mathematical methodology called stereology [22], originally developed to understand the 3D geologic composition of the earth from core samples. Stereology is now routinely used in histology (study of tissues or cells using a microscope [34]) to infer 3D structure from small samples or biopsies. In stereology, two-

dimensional images are viewed as projections of three-dimensional objects. Stereology relates three-dimensional parameters of structures to two-dimensional measurements that are obtained from 2D slices through the structures [22]. A variety of geometric attributes of follicles can be calculated using stereology, such as the follicle count, distribution of follicles within the ovary, and follicle size.

The quantitative properties of the ovary with respect to the follicles can be described by their volume density, surface density, numerical density, and the mean follicle dimension. Volume density is defined as the volume of the phase within the unit volume of the structure, surface density is surface area of the phase within unit volume of the structure, and numerical density is the number of follicles in the structure [22].

In stereology, volume density of a component is calculated as the ratio of the sum of component profile areas to the sum of the sectional area of the structure following the Principle of Delesse, where profile area means the area of the object cross-section or the area of the component cross-section, and section area means the area of the structure cross-section, where the area is calculated using a stereological method called the point counting method.

The areal density and thereby the volume density of objects in a given slice is determined by summing up the individual profile areas, where the area of a profile in stereologic measurement is computed using point counting method, which is explained in Chapter 2.

This stereologic method is commonly used on histological slices, but for digital images, this method of area calculation can be replaced with an automatic area estimation of the segmented and labelled follicles in Matlab R2006a. The section area of a structure is calculated as:

$$sectionArea = width(columns) \times height(rows) \tag{4.4}$$

where the width and height attributes of the image region can be obtained using a function called *imattributes* in Matlab R2006a, which returns an array with the image information. The object profile area is calculated using a Matlab function *bwarea* as $profileArea = bwarea(follicles)$, where *bwarea* estimates the area of the objects in binary image and $follicles$ represent the segmented follicle regions in the binary image. Thus, the areal

density (volume density) of the follicle profiles can be calculated as

$$volumeDensity(VD) = \frac{profileArea}{sectionArea}. \tag{4.5}$$

Surface density S_v is defined as the amount of surface area S_a contained in unit volume of tissue V_c. In stereology, surface density is estimated as $(4/\pi)\times$boundary density [22], where boundary density is the ratio of the length of follicle boundary (B_a) to the section area. Length of the follicle boundary was calculated by counting the number of pixels that make up the boundary of the follicle region, and was calculated using Matlab as given below.

```
[B] = bwboundaries(follicles,8,'noholes')
for k = 1 to length(B) do
    boundary = B{k};
    count = count + length(boundary);
end for
```

where *bwboundaries* traces the exterior boundaries of objects(follicles), in the binary image $follicles$. Thus, boundary density was estimated as $\frac{count}{sectionArea}$, and surface density was estimated as $\frac{4}{\pi}\times$ boundary density.

Numerical density (number of follicle regions per unit area) was obtained by counting the number of follicles in the ultrasonographic image. Follicle size was calculated by computing the average diameter of all the follicle regions in the given image. This was achieved by finding the equivalent diameter of a circle with the same area as a follicle region and was computed as $\sqrt{4*Area/\pi}$. It can also be computed automatically using Matlab function $EquivDiameter$.

The five quantitative descriptors were thus calculated for the segmented follicles of the given ultrasonographic images and were used as follicle features for the final classification step. The following five stereological features were used to construct a feature vector describing the follicles segmented from the input image: 1) surface density (SD); 2) volume density (VD); 3) number of follicle regions per image (Profiles); 4) mean follicle diameter (meanD); and, 5) maximum follicle diameter (maxD). These features were chosen because they characterize the most important aspects of follicles within the ovary and

Table 4.1: Mean and standard deviation of the feature vectors surface density(SD), volume density (VD), number of follicle profiles, mean and maximum diameters extracted from polycystic ovaries.

μ and σ	SD	VD	Profiles	Mean Diameter	Max Diameter
$Mean(n = 33)$	0.0304	0.1354	11	24.37 mm	42.66 mm
σ	0.12	0.06	5	3.69 mm	10.74 mm

Table 4.2: Mean and standard deviation of the feature vectors surface density(SD), volume density (VD), number of follicle profiles, mean and maximum diameter extracted from expert traced polycystic ovaries.

μ and σ	SD	VD	Profiles	Mean Diameter	Max Diameter
$Mean(n = 32)$	0.0302	0.1504	13	25.50 mm	37.59 mm
σ	0.0084	0.05	4	4.45 mm	7.86 mm

abnormalities in follicle morphology are a primary indication of PCO. Table 4.1 contain feature vectors extracted from images of polycystic ovaries obtained after the segmentation and feature extraction (stereology) phases. Table 4.3 contain feature vectors extracted from normal ovaries. Table 4.2 and table 4.4 contain feature vectors extracted from expert traced PCO and normal ovaries respectively. In table 4.3 and table 4.1, *SD* denotes the surface density and VD denotes the volume density. Figure 4.1 shows a scatter plot of the population of feature observations of PCO and normal ovaries, where the red x denote the normal feature plots and the blue o represent the PCO feature plots. Each individual set of axes in the figure contains a scatter plot of the columns of the feature observations against each other, grouped into two classes as normal and PCO, where the columns are a set of observations of a single feature over multiple samples. That is, column one is surface density(SD), column two is volume density (VD), column three is the number of follicle profiles, column four is the mean follicle diameter, and column five is the maximum follicle diameter over multiple samples of normal and PCO ovaries. For example, for the axis SD versus maxD, the scatter plot plots the population of observed SD obser-

Table 4.3: Mean and standard deviation of the feature vectors surface density(SD), volume density (VD), number of follicle profiles, mean and maximum diameters extracted from normal ovaries.

μ and σ	SD	VD	Profiles	Mean Diameter	Max Diameter
$Mean(n = 37)$	0.0224	0.1244	6	32.60 mm	48.06 mm
σ	0.01	0.05	3	12 mm	21.38 mm

Table 4.4: Mean and standard deviation of the feature vectors surface density(SD), volume density (VD), number of follicle profiles, mean and maximum diameters extracted from expert traced normal ovaries.

μ and σ	SD	VD	Profiles	Mean Diameter	Max Diameter
$Mean(n = 36)$	0.0166	0.1347	4	41.01 mm	60.02 mm
σ	0.0068	0.07	2	20.66 mm	33.87 mm

vations versus MaxD observations for each of the classes. The five columns against each other gives 25 set of axes. Each plot in the upper triangular block of plots corresponds to a plot in the lower triangular block of plots that is itself flipped about the line $y = x$. For example, the plot of SD versus maxD is the same as the plot of maxD vs SD flipped about the line $y = x$. The five diagonal axes starting from the top left to the bottom right are the histograms of SD, VD, number of follicle profiles, mean follicle diameter, and maximum follicle diameter respectively for both the PCO and the normal features combined. This scatter plot helps to infer the distribution of the PCO and the normal feature observations. For example, the axis maxD versus SD shows that PCO features dominate the second half of the SD axis; that is, have higher surface densities, but have lower values for the maximum diameter. From the same axis, it can also be inferred that normal features have higher values for the maximum diameter but have smaller values for SD. Each set of indices can be thus interpreted to study the correlation of the PCO and the normal feature observations against the five different features.

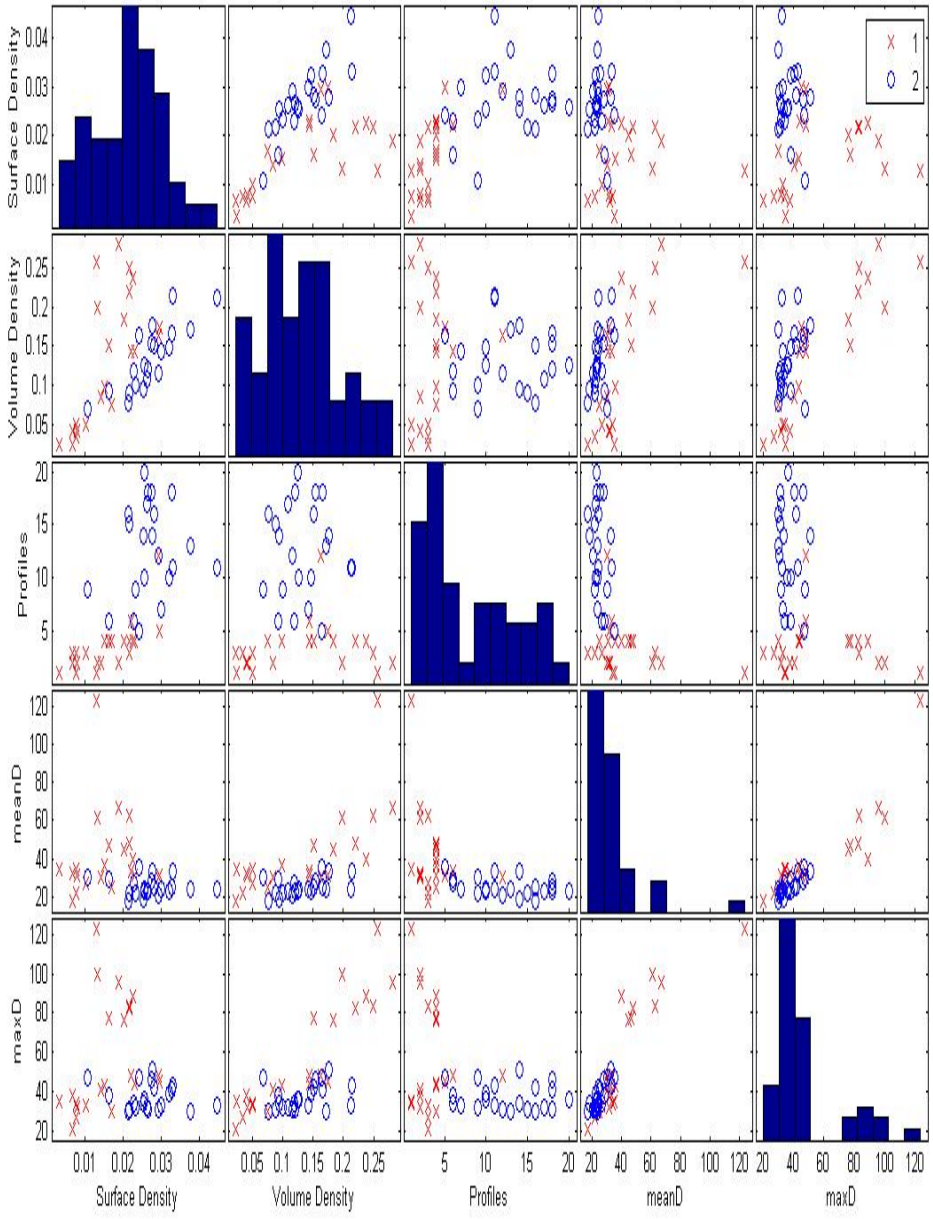

Figure 4.1: Scatter plots of the set of feature observations of PCO and normal ovaries: Each individual set of axes contain a scatter plot of the columns of the feature observations against each other, grouped as normal and PCO. Red x represent the normal features and the blue o represent the PCO features. The diagonal axes are the histograms of SD, VD, number of follicle profiles, mean follicle diameter, and maximum follicle diameter for both the PCO and the normal features combined.

4.3 Classification

The feature vectors obtained from the previous step were classified into one of the following two classes: (i) PCO present; or, (ii) PCO absent. The linear discriminant classifier, k-nearest neighbor classifier (KNN), and Support Vector Machine (SVM) classifier available in Matlab R2006a Bioinformatics toolbox (The Mathworks, Inc) were evaluated for their ability to correctly determine classes of feature vectors. The classification rates of each classifier were determined using k-fold cross validation methodology (Matlab function *crossvalind*).

4.4 Follicle distribution

An algorithm was devised to automatically classify the spatial distribution of follicles in an ovary as either random or peripheral. For each ovary, the centroid of each segmented region was found. The mean centroid (centroid of the centroids), denoted m_c, also was computed. The mean and standard deviation of the distances between each region centroid and m_c were used as features for this classification. Higher order moments such as skew and kurtosis of region centroid distances to m_c were not found to improve the classification results presented below. The classification was performed on 23 PCO ovaries, of which 11 were peripherally distributed and 12 were randomly distributed. The features were extracted and classification was performed using the linear discriminant classifier and the KNN classifier. Figure 4.2 shows the follicle centroids, where the blue stars represent the follicle centroid, and the green circle is the mean centroid or the centroid of the centroids.

4.5 Experimental Setup

The ovarian ultrasonographic images were obtained from the Women's Health Imaging Research Laboratory (WHIRL) in Saskatoon, Canada. This set contained images of both polycystic ovaries ($n = 33$) and normal ovaries ($n = 37$). These images were chosen from 19 normal patients and 10 PCOS patients. Pair of ovaries were not considered as a single

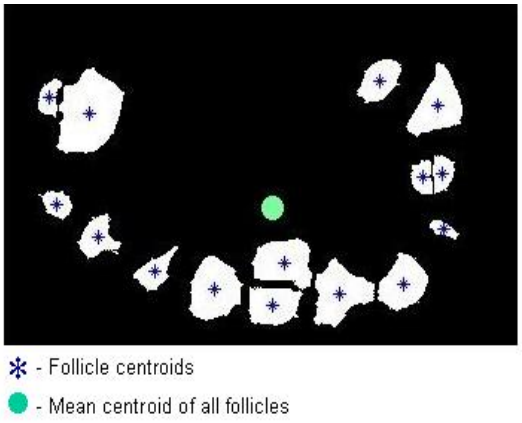

Figure 4.2: Centroids of the follicle regions

unit. That is, these images are either from the right or the left ovary of each patient, and were picked randomly. The region corresponding to the ovary were then manually segmented from these ultrasound images before being input to the software. A feature vector was extracted from each image using phases 1 and 2 of our algorithm (see Sections 4.1 and 4.2).

The 70 feature vectors were randomly divided into $k = 10$ folds for evaluation using the k-fold cross validation technique. Comparison of the classifier performance and classification results were done using this cross validation method.

CHAPTER 5

RESULTS AND DISCUSSION

5.1 Results and Discussion

Since the segmentation algorithm used to identify follicles was a slightly modified version of the algorithm in [2], a segmentation validation was performed to verify the accuracy of the modified algorithm. This process is detailed in Section 5.1.1. Section 5.1.2 presents the classification results for the three classifiers. Section 4.4 discusses results of a small experiment to classify the spatial distribution of follicles as random or peripheral automatically (as described in Section 2.2) using the linear discriminant and KNN classifiers.

5.1.1 Segmentation validation

The accuracy of follicle segmentation was measured by comparing manual segmentations generated by a human expert (ground truth) with our automatic segmentation results using the following similarity metrics: Hausdorff distance (HDist), mean distance (MDist), and DICE coefficient (DICE).

Hausdorff distance measures the largest minimum distance between a point on the automatically segmented region and all the points on the expert marked region and vice versa. It characterizes the maximum deviation of the segmentatation boundary from the ground truth. Let A denote the set of points in the automatically generated boundary and let G denote the set of points in the ground truth boundary. The Hausdorff distance is then

given by

$$d(p,B) = \min_{b\in B} ||b-p||, \tag{5.1}$$

$$\text{HDist} = \max\left[\max_{a\in A}[d(a,G)], \max_{g\in G}[d(g,A)]\right], \tag{5.2}$$

where $d(p,B)$ is the minimum Euclidian distance between a point p and the boundary B. Thus, a smaller Hausdorff distance indicates a more accurate segmentation. The average Hausdorff distance for all the automatically segmented follicles was 46.16 pixels.

Mean distance (Mdist) is the average minimum distance between a point on A and the boundary G. It is formally defined as:

$$\text{MDist} = \frac{1}{2}\left[\frac{1}{n_A}\sum_{a\in A} d(a,G) + \frac{1}{n_G}\sum_{g\in G} d(g,A))\right], \tag{5.3}$$

where n_A is the total number of pixels in the segmented region and n_G is the total number of pixels in the expert traced region. The average MDist for all the automatically segmented follicles was 7.65 pixels. This result, combined with the average Hausdorff distance of 46.16 indicates there were few long segments of follicle boundaries that exhibited significant deviation from the ground truth.

The DICE coefficient is defined as the ratio of the area of intersection between the automatically segmented region A and the ground truth region G to one half of the total area of the automatically segmented and the expertly segmented regions:

$$DICE = \frac{A\cap G}{0.5(|A|+|G|)}. \tag{5.4}$$

This characterizes the percentage of ovarlap between the two regions. For our images, the average percentage of overlap between the automatically segmented images and the expert segmented images was found to be 62.39%.

Figure 5.1 depicts example automatic segmentations. The output of automatic segmentation is similar to the manually traced expert segmentation. Table 5.1 summarizes the segmentation validation results. A common mode of error is the division of single follicles into multiple regions.

The recognition rate (RR) and misidentification rate (MR) also were computed in order to characterize the ability of the segmentation algorithm to locate follicle regions regardless of the boundary accuracy. Recognition rate is the ratio of the number of actual follicles

in the ground truth that correspond to some automatically segmented follicle to the actual number of expert traced follicles. The number of follicles in the segmented image that corresponds with an actual expert traced follicle is counted for each image. That is, these follicles (obtained from automatic segmentation) overlap with follicles from the expert traced image. The ratio of this count to the total count of expert traced follicles in a given image, multiplied by 100 gives the recognition rate of the automatically segmented follicles in each image. This is computed by first finding the maximum number of regions in the expert traced image. The different regions are numbered by giving each region a label.

1: **for** i=region 1 to n **do**
2: Get the indices of the expert traced label image that correspond to region i
3: For the above indices get the corresponding value in the intersection label image, where intersection image is the image obtained by & operation of expert traced and automatically segmented image
4: Get the unique, non-zero elements(labels) from the above labels: $UNIQNONZERO$
5: **if** $UNIQNONZERO >= ONELABEL$ and DICE coefficient (combined of all labelled regions in intersection label image corresponding to region i of expert traced image) $>50\%$ **then**
6: Increment follicle intersect count. That is, consider that follicle recognized
7: **end if**
8: **end for**
9: Recognition Rate (RR) $= \frac{follicleintersectcount}{countofofexperttracedfollicles} \times 100$
10: Misidentification Rate (MR) $= \frac{countofauto.segmentedfollicles - follicleintersectcount}{countofofauto.segmentedfollicles} \times 100$

The average recognition rate for all our images was 83%. The original method of [2] achieved a RR of 78%.

The misidentification rate is defined as the proportion of the total number of segmented regions that did not correspond to an expert-identified follicle (false positives). It gives an indication of the regions that have been marked as a follicle by the automatic segmentation algorithms but that does not correspond to the expert traced follicle. As can be seen from the formulae of MR from the above algorithm, misidentification rate increases as the count of automatically segmented follicles that do not correspond to the expert traced

Table 5.1: Mean validation metrics for the automatic segmentation algorithm over all follicles in the data set.

Mean HDist	46.16 pixels
Mean MDist	7.65 pixels
Mean DICE	62.39%
Mean RR	83%
Mean MR	26.13%

follicle increases (numerator of the MR formulae). Oversegmentation of follicles in the segmentation step was a major contributer to the misidentification rate because it increased the count of the segmented follicles that do not correspond to the expert traced follicle. In oversegmentation, what experts perceive as a single follicle is split into two or more by the segmentation algorithm due to the way homogeneous regions are selected, and region growing is executed, thereby contributing a higher value to the numerator of the MR formulae.

The average MR for our images was 26.13%. The original algorithm had an MR of 29% [2].

5.1.2 Classification results

The accuracy of the classification of the feature vectors as polycystic or normal by the three classifiers as determined by the *k*-fold cross validation method is given in Table 5.2. Sensitivity is the proportion of polycystic ovaries for which there was a positive test. The linear discriminant classifier exhibited a sensitivity of 90.90% and the KNN classifier exhibited a sensitivity of 93.94%.

Specificity is defined as the proportion of disease-free ovaries for which there was a negative test. Consistently high rates of specificity were exhibited by all three classfiers. The linear discriminant classifier achieved the best sensitivity of 94.59%.

CorrectRate in Table 5.2 is the overall classification rate and indicates the percentage of ovaries for which a correct classification was made. The linear discriminant classifier

Table 5.2: Performance results for the linear discriminant (LDC), *k*-nearest neighbor (KNN) and support vector machine (SVM) PCO classifiers.

Classifier	CorrectRate	Sensitivity	Specificity
LDC	0.9286	0.9091	0.9459
KNN	0.9143	0.9394	0.8919
SVM	0.9143	0.9091	0.9189

Table 5.3: Follicle distribution.

Classifier	CorrectRate	Sensitivity	Specificity
LDC	0.8125	0.9167	0.5000
KNN	0.6250	0.7500	0.2500

produced the highest classification rate of 92.86%, while the KNN and SVM classifiers made correct decisions 91.43% of the time.

Table 5.3 shows the results of the follicle distribution classification using a linear discriminant classifier, and *k*-nearest neighbor classfier as determined by 10-fold cross validation. A correct classification rate of 81.2% was obtained using the linear discriminant classifier.

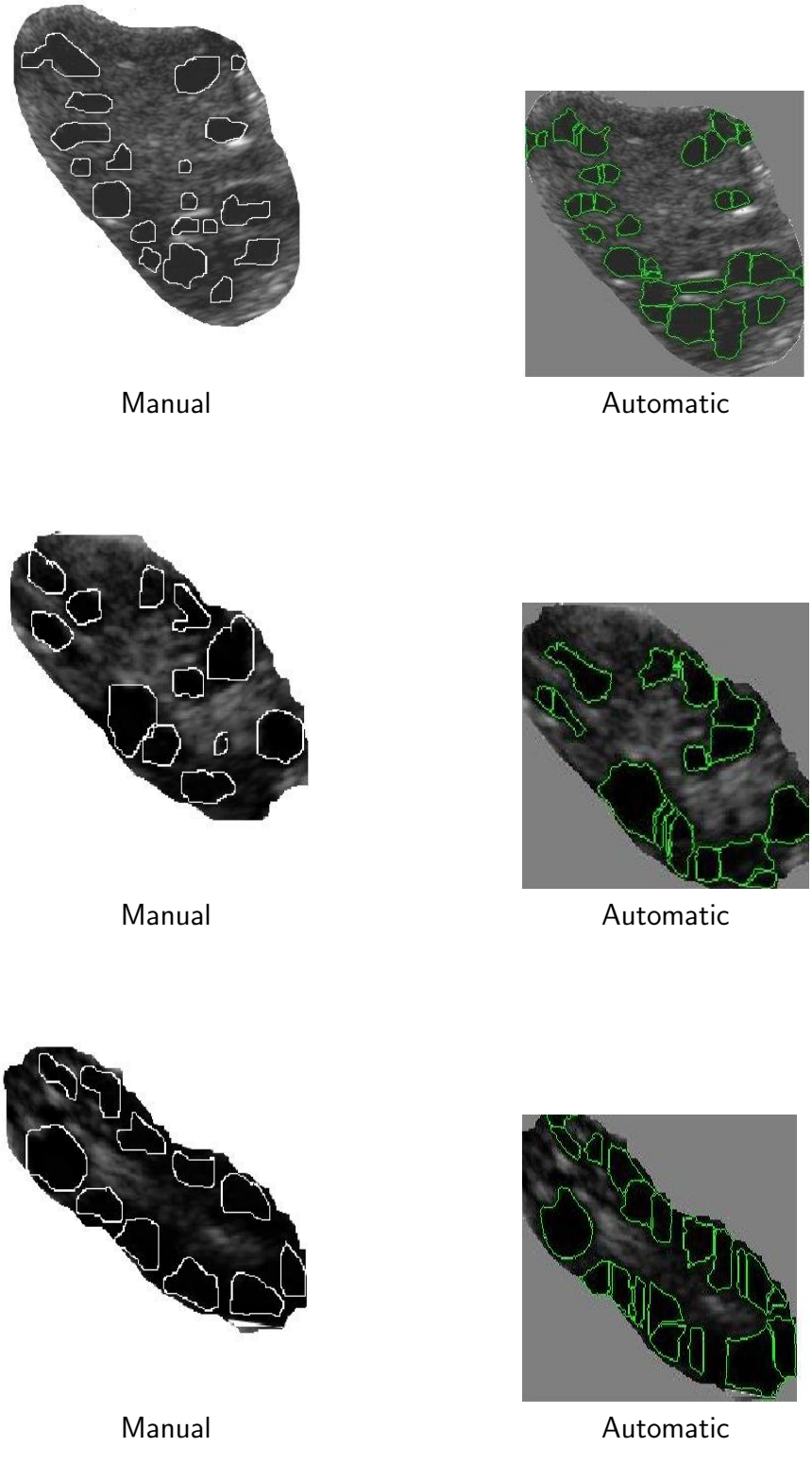

Figure 5.1: Examples of automatic segmentation results

CHAPTER 6

CONCLUSION AND FUTURE WORK

A method for automatically discriminating between normal ovarian follicle morphology and follicle morphology in polycystic ovaries was done in three phases: 1) Follicle segmentation using a region growing method; 2) quantification of the attributes of the segmented follicles using stereology; and 3) classification of the resulting feature vectors as either normal or polycystic. A slightly modified version of the algorithm in [2] was used for performing the automatic follicle segmentation, and feature vectors for the automatically segmented follicles were obtained using stereologic techniques that are commonly used in applications that need to obtain three dimensional attributes from two dimensional histological sections. We used the stereological quantitative descriptors to obtain the features from the follicle regions, but replaced the stereological techniques with some automated functions available in Matlab R2006a. The follicle feature vectors were then analyzed using three different classifiers: 1) linear discriminant; 2) KNN; and 3) SVM classifier. All the three classifiers performed well. Classification rates were 92.8%, 91.4%, 91.4%, respectively.

A classifier to analyze the distribution of the follicles inside polycystic ovaries was developed. It used two features, the mean and standard deviations of the distances of the centroids of individual follicles to the mean centroid. A linear discriminant classifier had a classification rate of 81% as determined by 10-fold cross validation.

Our results offer the promise of deploying a robust automated screening system for polycystic ovary morphology which will improve the rapidity and accuracy of diagnosis of Polycystic Ovarian Syndrome and facilitate early diagnosis and therefore reduced risk from the severe complications that can arise from this undiagnosed condition. This thesis has appeared in [35].

6.1 Future Work

A common mode of error in the automatic segmentation algorithm is the division of single follicles into multiple regions. This problem could be targeted in the future work which would help to increase the recognition rate and decrease the misidentification rate. Classification accuracy could be tested by adding more features to the feature set and by increasing the sample size to see if improvement can be achieved. Finally, future work on automatically segmenting the ovary region will improve the overall time, and the whole system could be setup as an add-on to an ultrasound machine with no manual interaction needed at any stage. Thus, all the ovarian ultrasonographic images taken for follicle analysis could be automatically added as a data set to the classifier and with time, the training data for the classifier would keep increasing thereby improving the classifier performance as well. Also, the time taken for the diagnosis will improve as the patient and their physicians would know the results of the scan instantly.

REFERENCES

[1] Adam Balen, Joop Laven, Seang-Lin Tan, and Didier Dewailly. Ultrasound assessment of the polycystic ovary: International consensus definitions. *Human Reproduction Update*, 9(6):505–514, 2003.

[2] Bozidar Potočnik and Damjan Zazula. Automated analysis of a sequence of ovarian ultrasound images. Part I: Segmentation of single 2D images. *Image and Vision Computing*, 20(3):217–225, 2002.

[3] Ching-Fen Jiang and Mu-Long Chen. Segmentation of Ultrasonic ovarian images by texture features. In *Proceedings of the 20th Annual International Conference of the IEEE Engineering in Medicine and Biology Society*, volume 2, pages 850–853, 1998.

[4] Yair Zimmer, Ron Tepper, and Solange Akselrod. Computerized quantification of structures within ovarian cysts using ultrasound images. *Ultrasound in Medicine and Biology*, 25(2):189–200, 1999.

[5] Memorial University of Newfoundland. Newfoundland and Canada Labrador. URL: `http://www.med.mun.ca/anatomyts/repro/arepro5.htm`; last accessed April 13, 2008.

[6] Wikimedia Commons;Order of changes in ovary. URL: `http://en.wikipedia.org/wiki/Image:Order_of_changes_in_ovary.svg`; last accessed April 17, 2008.

[7] Memorial University of Newfoundland. Newfoundland and Canada Labrador. URL: `http://www.med.mun.ca/anatomyts/repro/Repro55.gif`; last accessed April 13, 2008.

[8] Dr. Herring, Vice-Chairman, and Radiology Residency Program Director. URL: `http://www.learningradiology.com/caseofweek/caseoftheweekpix2006/cow190.jpg`; last accessed March 8, 2008. Albert Einstein Medical Center, Philadelphia, Pennsylvania.

[9] Texas Tech University Health Sciences Center School of Medicine. Polycystic ovary syndrome: Live images. URL: `http://www.macmed.ttuhsc.edu/Graham/gyn2/pages/newpage5.htm`; last accessed November 2006.

[10] Gordon Sarty, Weidong Liang, Milan Sonka, and Roger Pierson. Semiautomated segmentation of ovarian follicular ultrasound images using a knowledge-based algorithm. *Ultrasound in Medicine and Biology*, 24(1):27–42, 1998.

[11] DTREG Predictive Modeling Software. Linear discriminant analysis. URL: `http://www.dtreg.com/lda.htm`; last accessed March 8, 2008.

[12] Pattern recognition: Support vector machines. URL: `http://en.wikipedia.org/wiki/Support_vector_machine`; last accessed March 8, 2008.

[13] Stephen Franks. Medical Progress: Polycystic ovary syndrome. *New England Journal of Medicine*, 333(13):853–861, 1995.

[14] Abdulmalik Bako, Sharon Morad, and William Atiomo. Polycystic ovary syndrome: An overview. *Reviews in Gynaecological practice*, 5(2):115–122, 2005.

[15] Scott Chappel and Colin Howles. Re-evaluation of the roles of LH and FSH in the ovulatory processs. *Human Reproduction*, (6):1206–1212, 1991.

[16] J. Fortune, Robert Cushman, Christina Wahl, and S. Kito. The primordial to primary follicle transition. *Molecular and Cellular Endocrinology*, 163:53–60, 2000.

[17] Angela Baerwald, Gregg Adams, and Roger Pierson. A new model for ovarian follicular development during the human menstrual cycle. *Fertility and Sterility*, 80:116–122, 2003.

[18] Wendy Chang, Eric Knochenhauer, Alfred Bartolucci, and Ricardo Azziz. Phenotypic spectrum of polycystic ovary syndrome: Clinical and Biochemical characterization of the three major clinical subgroups. *Fertility and Sterility*, 83(6):1717–1723, 2005.

[19] Sophie Jonard, Yann Robert, Christine Cortet-Rudelli, Pascal Pigny, Christine Decanter, and Didier Dewailly. Ultrasound examination of polycystic ovaries: is it worth counting the follicles. *Human Reproduction*, 18(3):598–603, March 2003.

[20] William Hendee and E.Russell Ritenour. *Medical Imaging Physics*. Wiley-Liss, 4th edition, 2002.

[21] Russell Hobbie. *Intermediate Physics for Medicine and Biology*. John Wiley&Sons, 2nd edition, 1988.

[22] Ewald Weibel. *Stereological Methods. Vol. 1: Practical Methods for Biological Morphometry*. Academic Press, London, U.K., 1979.

[23] Anthony Krivanek and Milan Sonka. Ovarian ultrasound image analysis: Follicle segmentation. *IEEE Transactions on Medical Imaging*, 17(6):935–944, 1998.

[24] Russell Muzzolini, Yee-Hong Yang, and Roger Pierson. Multiresolution Texture Segmentation with Application to Diagnostic Ultrasound Images. *IEEE Transactions on Medical Imaging*, 12(1):108–123, 1993.

[25] Bozidar Potočnik and Damjan Zazula. Automated analysis of a sequence of ovarian ultrasound images. Part II: Prediction-based object recognition from a sequence of images. *Image and Vision Computing*, 20(3):227–235, 2002.

[26] Barbara Levienaise-Obadia and Andrew Gee. Adaptive segmentation of ultrasound images. *Image and Vision Computing*, 17:583–588, 1999.

[27] Na Harrington. Segmentation of human ovarian follicles from ultrasound images acquired in vivo using geometric active contour models and a Naive Bayes classifier. Master's thesis, Department of Computer Science, University of Saskatchewan, 2007.

[28] Yair Zimmer, Ron Tepper, and Solange Akselrod. A two-dimensional extension of minimum cross entropy thresholding for the segmentation of ultrasound images. *Ultrasound in Medicine and Biology*, 22(9):1183–1190, 1996.

[29] Mehdi Moradi, Parvin Mousavi, and Purang Abolmaesumi. Computer-aided diagnosis of prostate cancer with emphasis on ultrasound-based approaches: A review. *Ultrasound in Medicine and Biology*, 33(7):1010–1028, 2007.

[30] Luc Vincent and Pierre Soille. Watersheds in digital spaces: An efficient algorithm based on immersion simulations. *IEEE Transactions on Pattern Analysis and Machine Intelligence*, 13:583–598, 1991.

[31] Jack Baskin School of Engineering; University of California Santa Cruz. Fisher's linear discriminant. URL: `http://www.soe.ucsc.edu/research/compbio/genex/genexTR2html/node12.html`; last accessed March 8, 2008.

[32] Pattern recognition: K-nearest neighbor algorithm. URL: `http://en.wikipedia.org/wiki/Nearest_neighbor_pattern_recognition`; last accessed March 8, 2008.

[33] Kevin W. Bowyer. Validation of medical image analysis techniques. In Milan Sonka and J. M. Fitzpatrick, editors, *Handbook of Medical Imaging*, volume 2, chapter 10. SPIE-International Society for Optical Engineering, 2000.

[34] Don Fawcett and William Bloom. *Bloom and Fawcett: A Textbook of Histology*. Hodder Arnold, 12th edition, 1994.

[35] Maryruth J. Lawrence, Mark G. Eramian, Roger A. Pierson, and Eric Neufeld. Computer assisted detection of polycystic ovary morphology in ultrasound images. In *CRV*, pages 105–112, 2007.